Received 10 April 2024; revised 9 May 2024; accepted 17 May 2024. Date of publication 11 June 2024; date of current version 31 July 2024.
The review of this paper was arranged by Associate Editor Mohammad Tayeb Al Qaseer.

Digital Object Identifier 10.1109/OJIM.2024.3412205

Microwave NDT/NDE Through Differential Bayesian Compressive Sensing

MARCO SALUCCI [1,2] (Senior Member, IEEE), LORENZO POLI [1,2] (Senior Member, IEEE), GIORGIO GOTTARDI [1,2], GIACOMO OLIVERI [1,2] (Fellow, IEEE), LUCA TOSI [1,2] (Member, IEEE), AND ANDREA MASSA [1,2,3,4,5] (Fellow, IEEE)

(Invited Paper)

[1]ELEDIA Research Center (ELEDIA@UniTN - University of Trento), DICAM - Department of Civil, Environmental, and Mechanical Engineering, 38123 Trento, Italy

[2]CNIT - "University of Trento" ELEDIA Research Unit, 38123 Trento, Italy

[3]ELEDIA Research Center (ELEDIA@UESTC - UESTC), School of Electronic Science and Engineering, University of Electronic Science and Technology of China, Chengdu 611731, China

[4]ELEDIA Research Center (ELEDIA@TSINGHUA - Tsinghua University), Beijing 100084, China

[5]School of Electrical Engineering, Tel Aviv University, Tel Aviv 69978, Israel

CORRESPONDING AUTHOR: A. MASSA (e-mail: andrea.massa@unitn.it)

This work benefited from the networking activities carried out within the Project "Hub Life Science - Advanced Diagnosis (HLS-AD), PNRR PNC-E3-2022-23683266 PNC-HLS-DA, INNOVA" funded by the Italian Ministry of Health under the National Complementary Plan Innovative Health Ecosystem (CUP: E63C22003780001 - Unique Investment Code: PNC-E.3), the Project "AURORA - Smart Materials for Ubiquitous Energy Harvesting, Storage, and Delivery in Next Generation Sustainable Environments" funded by the Italian Ministry for Universities and Research within the PRIN-PNRR 2022 Program (CUP: E53D23014760001) , the Project "Telecommunications of the Future" (PE00000001 - program "RESTART," Structural Project 6GWINET), funded by European Union under the Italian National Recovery and Resilience Plan (NRRP) of NextGenerationEU (CUP: D43C22003080001), the Project "Telecommunications of the Future" (PE00000001 - program "RESTART," Focused Project MOSS), funded by European Union under the Italian National Recovery and Resilience Plan (NRRP) of NextGenerationEU (CUP: J33C22002880001), the Project "Telecommunications of the Future" (PE00000001 - program "RESTART," Structural Project IN), funded by European Union under the Italian National Recovery and Resilience Plan (NRRP) of NextGenerationEU (CUP: J33C22002880001), the Project "INSIDE - NEXT - Indoor Smart Illuminator for Device Energization and Next-Generation Communications" Funded by the European Union under NextGenerationEU (CUP: E53D23000990001), and the Project "ICSC National Centre for HPC, Big Data and Quantum Computing (CN HPC)" funded by the European Union - NextGenerationEU within the PNRR Program (CUP: E63C22000970007). Views and opinions expressed are however those of the author(s) only and do not necessarily reflect those of the European Union or the European Research Council. Neither the European Union nor the granting authority can be held responsible for them.

ABSTRACT This article deals with the nondestructive testing and evaluation (NDT/NDE) of dielectric structures through a sparseness-promoting probabilistic microwave imaging (MI) method. Prior information on both the unperturbed scenario and the class of imaged targets is profitably exploited to formulate the inverse scattering problem (ISP) at hand within a differential contrast source inversion (CSI) framework. The imaging process is then efficiently completed by applying a customized Bayesian compressive sensing (BCS) inversion strategy. Selected numerical and experimental results are provided to assess the effectiveness of the proposed imaging method also in comparison with competitive state-of-the-art alternatives.

INDEX TERMS Bayesian compressive sensing (BCS), differential imaging, inverse scattering problem (ISP), microwave imaging (MI), nondestructive testing and evaluation (NDT/NDE).

I. INTRODUCTION AND MOTIVATION

ELECTROMAGNETIC (EM) fields at microwave frequencies can be profitably used to perform, also contactless, inspections of materials with good spatial resolution and nonionizing effects [1], [2]. More specifically, microwave imaging (MI) techniques are aimed at noninvasively reconstructing the dielectric properties of an inaccessible domain by means of low-cost, portable, and safe

© 2024 The Authors. This work is licensed under a Creative Commons Attribution-NonCommercial-NoDerivatives 4.0 License.
For more information, see https://creativecommons.org/licenses/by-nc-nd/4.0/

equipment, with applications including biomedical imaging [3], [4], [5], [6], [7], subsurface investigations [8], [9], through-wall imaging [10], [11], and nondestructive testing and evaluation (NDT/NDE) [12], [13], [14], [15], [16], [17], [18]. Concerning this latter, MI is a valid alternative to well-established technologies, such as eddy currents [19] and ultrasounds [20]. Moreover, the structural evaluation of composite low-permittivity/low-loss materials (e.g., foam, honeycombs, and glass fiber reinforced polymers [14]), without compromising their properties and functionalities, is an attractive field of research due to their increasing diffusion in modern aircrafts and radomes [21].

However, solving the underlying inverse scattering (IS) problem to yield a faithful diagnosis of the structure under test (SUT) in a reasonable amount of time, as well, is a very challenging task because of 1) the nonuniqueness of the IS solution due to the presence of nonradiating currents giving null/nonmeasurable contributions to the collectable field in the observation domain (i.e., outside the investigation domain) [22]; 2) the presence of local minima (false solutions) in the data mismatch cost function caused by the highly nonlinear nature of the scattering phenomena in the microwave regime [23]; and 3) the strong sensitivity to noise caused by the ill-conditioning [1]. While no practical solutions exist to avoid 1), the local minima issue 2) can be effectively mitigated by designing suitable measurement setups that collect all the available nonredundant information on the imaged domain according to the scattered field degrees-of-freedom theory [24]. Moreover, 1) linear approximations [25]; 2) synthetic-aperture radar (SAR)-based approaches [26]; 3) multiresolution schemes (IMSA) [27]; and/or 4) stochastic optimization algorithms [28], [29], [30] proved to be valid counter-measures, as well. However, strategies belonging to class a), such as the Born approximation [25], turn out to be reliable in those applications where a qualitative guess of the shape and location of the unknown targets is enough. Similar limitations affect the SAR methods b) since they can only retrieve reflectance/emittance images [26]. Many effective methods have been developed exploiting IMSAs c) in combination with both deterministic and stochastic solvers to reduce the ratio between unknowns and data as well as to adaptively enhance the image resolution only within the so-called regions-of-interest (RoIs). Finally, the solution approaches based on multiagent strategies d) with "hill-climbing" properties, such as the particle swarm optimizer (PSO) [28], the differential evolution (DE) [29], and the genetic algorithm (GA) [31], [32], [33], are effective in sampling the solution spaces without being trapped into local minima, but they are generally prone to slow convergence and very high computational costs. This latter drawback has been partially overcome by introducing efficient tools for the prediction of the electric field (e.g., the Sherman–Morrison–Woodbury (SMW) formulation [33]) or exploiting the system-by-design (SbD) paradigm [34].

On the other hand, to effectively cope with iii), effective regularization strategies must be used [1]. Toward this end, suitable sources of a-priori information can be profitably exploited. In NDT/NDE inspections, the generally available knowledge on the unperturbed SUT can be taken into account in the IS formulation to recover only *differences* with respect to such a known scenario [11]. Furthermore, a-priori knowing the class of imaged defects/cracks in terms of their EM composition and/or shape can significantly help in regularizing the IS problem (ISP) at hand. This is the case of several state-of-the-art solutions based on GAs [31], [32], [33], as well as of parametric inversion methods formulated within the learning-by-examples (LBE) framework [19], [35] which are aimed at real-time estimating a set of predefined SUT descriptors thanks to the knowledge acquired from a training set of properly selected input/output pairs.

Otherwise, compressive sensing (CS) is an effective alternative to yield regularized solutions of the ISP thanks to the exploitation of *sparseness priors* on the unknown scatterers [21], [22], [25], [36], [37], [38], [39]. This work presents a novel CS-based technique—preliminarily presented and validated in [40]—to deal with the NDT/NDE inspection of dielectric structures when a-priori information on the unperturbed SUT is available. Toward this end, the MI-ISP at hand is suitably formulated within a *differential* contrast source inversion (CSI) framework [41], [42] to perform the offline computation of the inhomogeneous Green's operator of arbitrary SUTs, thus reaching a remarkable time saving. The retrieval of the unknown *differential* contrast sources is addressed in a *probabilistic* manner through a customized multitask Bayesian CS (MT-BCS) solver [37], [38] that enforces not only the *sparseness* of the solution but also the physical correlation existing between the differential currents induced by the different illuminations in a multiview inspection set-up.

The outline of this article is as follows. The mathematical formulation of the differential NDT/NDE problem is provided in Section II, while the proposed MT-BCS inversion approach is described in Section III. Section IV provides an extensive validation of the method through representative numerical and experimental test cases as well as with some comparisons with competitive state-of-the-art alternatives. Finally, some conclusions and final remarks are drawn in Section V.

II. MATHEMATICAL FORMULATION

With reference to the 2-D transverse magnetic (2D-TM) NDT/NDE scenario sketched in Fig. 1(a), let Γ be an investigation domain characterized by the following complex permittivity distribution:

$$\varepsilon(\mathbf{r}) = \begin{cases} \varepsilon_\Psi(\mathbf{r}), \text{ if } \mathbf{r} \in \Psi \subset \Gamma \\ \varepsilon_B(\mathbf{r}), \text{ otherwise}, \quad \mathbf{r} = (x,\, y) \in \Gamma \end{cases} \tag{1}$$

and immersed in a free-space background ($\varepsilon_0 \approx 8.85 \times 10^{-12}$ [F/m], $\mu_0 = 4\pi \times 10^{-7}$ [H/m], $\sigma_0 = 0$ [S/m]). In (1), $\Psi \subset \Gamma$ is the support (either simply connected or disconnected) of an

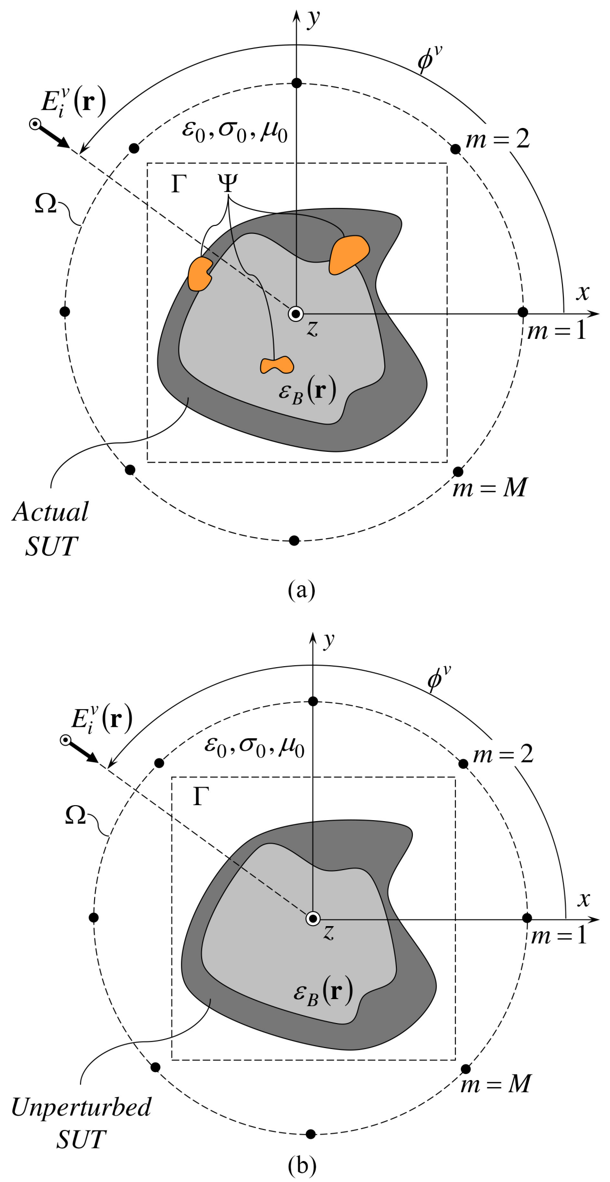

FIGURE 1. Geometry of the (a) actual and (b) unperturbed NDT/NDE scenario.

unknown object with complex permittivity at the frequency f[1] equal to

$$\varepsilon_\Psi(\mathbf{r}) = \varepsilon_0 \varepsilon_{r\Psi}(\mathbf{r}) - j\frac{\sigma_\Psi(\mathbf{r})}{2\pi f}. \tag{2}$$

$\varepsilon_{r\Psi}$ and σ_Ψ being the relative permittivity and the conductivity, respectively. Moreover, the unperturbed/reference SUT [Fig. 1(b)] is modeled by the inhomogeneous distribution in Γ

$$\varepsilon_B(\mathbf{r}) = \varepsilon_0 \varepsilon_{rB}(\mathbf{r}) - j\frac{\sigma_B(\mathbf{r})}{2\pi f}. \tag{3}$$

The investigation domain Γ is illuminated by a set of EM waves impinging from the V angular directions $\phi^v = (v-1)\times(2\pi/V)$ ($v = 1, \dots, V$), $E_i^v(\mathbf{r})$ being the vth ($v = 1, \dots, V$) associated z-polarized incident electric field. The arising EM interactions within Γ are governed by the *state* equation

$$E_i^v(\mathbf{r}) = E^v(\mathbf{r}) - j\frac{k_0^2}{4}\int_\Gamma \mathcal{H}\left(k_0\left|\mathbf{r}-\mathbf{r}'\right|\right)\tau\left(\mathbf{r}'\right)E^v\left(\mathbf{r}'\right)d\mathbf{r}'. \tag{4}$$

($v = 1, \dots, V$), where $E^v(\mathbf{r})$ is the vth ($v = 1, \dots, V$) total field, $k_0 = 2\pi f\sqrt{\varepsilon_0\mu_0}$, $\mathcal{H}(.)$ is the 0th-order Hankel function of second kind, $|\mathbf{r}-\mathbf{r}'| = \sqrt{(x-x')^2+(y-y')^2}$, and $\tau(\mathbf{r})$ ($\tau(\mathbf{r}) \triangleq [\varepsilon(\mathbf{r})/\varepsilon_0] - 1$) is the contrast function [Fig. 1(a)]. Moreover, the scattered field $E_s^v(\mathbf{r}_m) = [E^v(\mathbf{r}_m) - E_i^v(\mathbf{r}_m)]$ ($m = 1, \dots, M$, $v = 1, \dots, V$) collected at M probing locations $\mathbf{r}_m$ ($m = 1, \dots, ., M$) within an external observation domain Ω [$\Omega \cap \Gamma = \emptyset$—Fig. 1(a)] complies with the *data* equation

$$E_s^v(\mathbf{r}_m) = j\frac{k_0^2}{4}\int_\Gamma \mathcal{H}\left(k_0\left|\mathbf{r}_m-\mathbf{r}'\right|\right)\tau\left(\mathbf{r}'\right)E^v\left(\mathbf{r}'\right)d\mathbf{r}'. \tag{5}$$

($v = 1, \dots, V$). Similar equations hold true for the reference scenario [Fig. 1(b)] where the *state* ($\mathbf{r} \in \Gamma$) and *data* ($\mathbf{r}_m \in \Omega$) equations read as

$$\begin{aligned} E_i^v(\mathbf{r}) = E_B^v(\mathbf{r}) - j\frac{k_0^2}{4}\int_\Gamma &\mathcal{H}\left(k_0\left|\mathbf{r}-\mathbf{r}'\right|\right) \\ &\times \tau_B\left(\mathbf{r}'\right)E_B^v\left(\mathbf{r}'\right)d\mathbf{r}' \\ &v = 1, \dots, V \end{aligned} \tag{6}$$

and

$$\begin{aligned} E_{sB}^v(\mathbf{r}_m) = j\frac{k_0^2}{4}\int_\Gamma \mathcal{H}\left(k_0\left|\mathbf{r}_m-\mathbf{r}'\right|\right)\tau_B\left(\mathbf{r}'\right)E_B^v\left(\mathbf{r}'\right)d\mathbf{r}' \\ m = 1, \dots, M;\ v = 1, \dots, V \end{aligned} \tag{7}$$

respectively, $E_B^v(\mathbf{r})$ and $E_{sB}^v(\mathbf{r}_m)$ ($\triangleq [E_B^v(\mathbf{r}_m) - E_i^v(\mathbf{r}_m)]$) ($m = 1, \dots, M$) being the total and the scattered field of the background distribution modeled by the corresponding contrast function $\tau_B(\mathbf{r})$ ($\tau_B(\mathbf{r}) \triangleq [\varepsilon_B(\mathbf{r})/\varepsilon_0] - 1$). By subtracting (6) from (4), it is possible to isolate the contribution of the unknown target within Γ in terms of the *differential* field $E_D^v(\mathbf{r}) = [E^v(\mathbf{r}) - E_B^v(\mathbf{r})]$ ($\mathbf{r} \in \Gamma$; $v = 1, \dots, V$), which is given by

$$E_D^v(\mathbf{r}) = j\frac{k_0^2}{4}\int_\Gamma \mathcal{H}\left(k_0\left|\mathbf{r}-\mathbf{r}'\right|\right) \times \left[\tau_B\left(\mathbf{r}'\right)E_D^v\left(\mathbf{r}'\right) + J_D^v\left(\mathbf{r}'\right)\right]d\mathbf{r}' \tag{8}$$

where

$$J_D^v(\mathbf{r}) = \tau_D(\mathbf{r})E^v(\mathbf{r}) \tag{9}$$

is the vth ($v = 1, \dots, V$) unknown *differential* contrast source, while $\tau_D(\mathbf{r}) = [\tau(\mathbf{r}) - \tau_B(\mathbf{r})]$ is the *differential* contrast function ($\tau_D(\mathbf{r}) \neq 0$ for $\mathbf{r} \in \Psi$, $\tau_D(\mathbf{r}) = 0$ otherwise). Similarly, by subtracting (7) from (5), we yield the following vth ($v = 1, \dots, V$) relation at $\mathbf{r}_m \in \Omega$, $m = 1, \dots, M$:

$$\begin{aligned} E_D^v(\mathbf{r}_m) = j\frac{k_0^2}{4}\int_\Gamma &\mathcal{H}\left(k_0\left|\mathbf{r}_m-\mathbf{r}'\right|\right) \\ &\times\left[\tau_B\left(\mathbf{r}'\right)E_D^v\left(\mathbf{r}'\right) + J_D^v\left(\mathbf{r}'\right)\right]d\mathbf{r}'. \end{aligned} \tag{10}$$

[1]A time-dependency factor $\exp(-j2\pi ft)$ is assumed and omitted hereinafter.

To numerically solve the ISP at hand, Richmond's procedure [43] is applied to (8) and (10) by subdividing Γ into N square subdomains, $\{\Gamma_n;\ n = 1, \ldots, N\}$, centered at $\{\mathbf{r}_n;\ n = 1, \ldots, N\}$. Accordingly, (8) can be rewritten in matrix form as

$$\underline{E}_D^{v,\Gamma} = \underline{\underline{G}}_B^{\Gamma}\, \underline{J}_D^{v}. \tag{11}$$

($v = 1, \ldots, V$), where $\underline{E}_D^{v,\Gamma} = \{E_D^v(\mathbf{r}_n);\ n = 1, \ldots, N\}^{\mathrm{T}}$and $\underline{J}_D^v = \{J_D^v(\mathbf{r}_n);\ n = 1, \ldots, N\}^{\mathrm{T}}$, $.^{\mathrm{T}}$ being the transpose operator. Moreover, the matrix $\underline{\underline{G}}_B^{\Gamma}$ is given by

$$\underline{\underline{G}}_B^{\Gamma} = \left(\underline{\underline{I}} - \underline{\underline{G}}_0^{\Gamma}\, \underline{\underline{\tau}}_B\right)^{-1} \underline{\underline{G}}_0^{\Gamma} \tag{12}$$

where $\underline{\underline{G}}_0^{\Gamma}$ is the $(N \times N)$ free-space *internal* Green's matrix, whose (p, q)th $(p, q = 1, \ldots, N)$ entry is equal to $\underline{\underline{G}}_0^{\Gamma}\rfloor_{p,q} = j(k_0^2/4)\int_{\Gamma_q} \mathcal{H}(k_0|\mathbf{r}_p - \mathbf{r}'|)d\mathbf{r}'$ [1], $\underline{\underline{I}}$ is the identity matrix, and $\underline{\underline{\tau}}_B$ is a diagonal matrix (i.e., $\underline{\underline{\tau}}_B = \mathrm{diag}\{\underline{\tau}_B\}$) with $\underline{\tau}_B = \{\tau_B(\mathbf{r}_n);\ n = 1, \ldots, N\}$. Analogously, the discrete form of (10) turns out to be

$$\underline{E}_D^{v,\Omega} = \underline{\underline{G}}_0^{\Omega}\left(\underline{\underline{\tau}}_B\, \underline{\underline{G}}_B^{\Gamma} + \underline{\underline{I}}\right)\underline{J}_D^{v}. \tag{13}$$

($v = 1, \ldots, V$), where $\underline{E}_D^{v,\Omega} = \{E_D^v(\mathbf{r}_m) = [E^v(\mathbf{r}_m) - E_B^v(\mathbf{r}_m)];\ m = 1, \ldots, M\}$ and $\underline{\underline{G}}_0^{\Omega}$ is the $(M \times N)$ free-space *external* Green's matrix $(\underline{\underline{G}}_0^{\Omega}\rfloor_{m,n} = j(k_0^2/4)\int_{\Gamma_n} \mathcal{H}(k_0|\mathbf{r}_m - \mathbf{r}'|)d\mathbf{r}',\ m = 1, \ldots, M,\ n = 1, \ldots, N)$.

The NDT/NDE problem at hand can be then formulated as follows.

1) *NDT/NDE Differential CSI Problem Formulation:* Starting from the knowledge of the incident field, $\underline{E}_i^{v,\Gamma} = \{E_i^v(\mathbf{r}_n);\ n = 1, \ldots, N\}$ ($v = 1, \ldots, V$), of the unperturbed SUT ($\underline{\tau}_B$), and of the *differential* field samples ($\underline{E}_D^{v,\Omega}$), solve (13) subject to the hypothesis that the V unknown differential contrast sources, $\underline{J}_D^v$ ($v = 1, \ldots, V$), are a) *intrinsically sparse* with respect to the adopted set of N basis functions, $\{\psi_n(\mathbf{r});\ n = 1, \ldots, N\}$, being $\psi_n(\mathbf{r}) = 1$ if $\mathbf{r} \in \Gamma_n$ and $\psi_n(\mathbf{r}) = 0$ otherwise, and b) correlated.

III. SPARSITY-PROMOTING SOLUTION METHOD

Owing to the linear nature of (13) and the requirement that the solution is assumed to be *sparse* with respect to a suitable basis, the CS framework turns out to be a natural choice to yield regularized solutions of the ISP at hand [38]. Toward this end, (13) is rewritten as a real-valued system of equations as follows:

$$\underline{\Xi}^{v} = \underline{\underline{\chi}}\, \underline{\mathcal{J}}^{v};\quad v = 1, \ldots, V \tag{14}$$

where

$$\underline{\underline{\chi}} = \begin{bmatrix} \Re\left\{\underline{\underline{G}}_0^{\Omega}\left(\underline{\underline{\tau}}_B \underline{\underline{G}}_B^{\Gamma} + \underline{\underline{I}}\right)\right\} & -\Im\left\{\underline{\underline{G}}_0^{\Omega}\left(\underline{\underline{\tau}}_B \underline{\underline{G}}_B^{\Gamma} + \underline{\underline{I}}\right)\right\} \\ \Im\left\{\underline{\underline{G}}_0^{\Omega}\left(\underline{\underline{\tau}}_B \underline{\underline{G}}_B^{\Gamma} + \underline{\underline{I}}\right)\right\} & \Re\left\{\underline{\underline{G}}_0^{\Omega}\left(\underline{\underline{\tau}}_B \underline{\underline{G}}_B^{\Gamma} + \underline{\underline{I}}\right)\right\} \end{bmatrix}. \tag{15}$$

$\underline{\Xi}^v = [\Re\{\underline{E}_D^{v,\Omega}\}, \Im\{\underline{E}_D^{v,\Omega}\}]^{\mathrm{T}}$, and $\underline{\mathcal{J}}^v = [\Re\{\underline{J}_D^v\}, \Im\{\underline{J}_D^v\}]$, while $\Re\{.\}$ and $\Im\{.\}$ stand for the real and imaginary parts, respectively.

Since the solution of (14) with standard ℓ_1-based CS approaches is generally prevented because of the need to assess the compliancy of $\underline{\underline{\chi}}$ with the restricted isometry property (RIP), its computation being unfeasible when realistic values of M and N are considered [37], the MT-BCS method [44] is adopted to yield a maximally sparse prediction of the differential contrast sources ($\underline{\widetilde{\mathcal{J}}}^v = [\widetilde{\mathcal{J}}_n^v;\ n = 1, \ldots, 2 \times N]$, $v = 1, \ldots, V$). Such an alternative *probabilistic* CS-based approach determines the vth ($v = 1, \ldots, V$) unknown as

$$\underline{\widetilde{\mathcal{J}}}^{v} = \arg\left\{\max_{\underline{\mathcal{J}}^v}\left[\int \mathcal{P}\left(\underline{\mathcal{J}}^v|\underline{\Xi}^v, \underline{u}\right)\mathcal{P}\left(\underline{u}|\underline{\Xi}^v\right)d\underline{u}\right]\right\}. \tag{16}$$

$\mathcal{P}(\underline{\mathcal{J}}^v|\underline{\Xi}^v, \underline{u})$ and $\mathcal{P}(\underline{u}|\underline{\Xi}^v)$ being the a-posteriori probability and the hyperparameters posterior, respectively, while $\underline{u} = \{u_n;\ n = 1, \ldots, 2 \times N\}$ is the set of MT-BCS hyperparameters. According to (16), the same set $\underline{u}$ is shared among all the V views to enforce the underlying physical correlation among the differential contrast sources induced by the different illuminations. The closed-form solution of (16) is given by

$$\underline{\widetilde{\mathcal{J}}}^{v} = \left[\mathrm{diag}\left(\underline{\widetilde{u}}\right) + \underline{\underline{\chi}}^{\mathrm{T}}\,\underline{\underline{\chi}}\right]^{-1} \underline{\underline{\chi}}^{\mathrm{T}}\, \underline{\Xi}^{v}. \tag{17}$$

($v = 1, \ldots, V$) where the estimated values of the hyperparameters $\underline{u}$, $\underline{\widetilde{u}} = \{\widetilde{u}_n;\ n = 1, \ldots, 2 \times N\}$, are determined thanks to a fast relevance vector machine (RVM) solver [45] by solving the following maximization problem:

$$\underline{\widetilde{u}} = \arg\left\{\max_{\underline{u}}\left[-\frac{1}{2}\sum_{v=1}^{V} 2(M + \gamma_1) \times \log\left(\left(\underline{\Xi}^v\right)^{\mathrm{T}}\left(\underline{\underline{Q}}\right)^{-1}\underline{\Xi}^v + 2\gamma_2\right) + \log\left|\underline{\underline{Q}}\right|\right]\right\}. \tag{18}$$

In (18), (γ_1, γ_2) are the MT-BCS control parameters, while

$$\underline{\underline{Q}} = \underline{\underline{I}} + \underline{\underline{\chi}}\left[\mathrm{diag}\left(\underline{u}\right)\right]^{-1}\underline{\underline{\chi}}^{\mathrm{T}}. \tag{19}$$

Finally, the MT-BCS estimation of the contrast function turns out to be

$$\widetilde{\tau}(\mathbf{r}_n) = \tau_B(\mathbf{r}_n) + \frac{1}{V}\sum_{v=1}^{V}\frac{\widetilde{J}_D^v(\mathbf{r}_n)}{\widetilde{E}^v(\mathbf{r}_n)}. \tag{20}$$

($n = 1, \ldots, N$), $\underline{\widetilde{J}}_D^v = \{\widetilde{J}_D^v(\mathbf{r}_n) = (\widetilde{\mathcal{J}}_n^v + j\widetilde{\mathcal{J}}_{n+N}^v);\ n = 1, \ldots, N\}$ and $\underline{\widetilde{E}}^{v,\Gamma} = \{\widetilde{E}^v(\mathbf{r}_n);\ n = 1, \ldots, N\}$ being the vth ($v = 1, \ldots, V$) retrieved *differential* contrast source and total field, respectively. This latter is yielded by substituting $\underline{\widetilde{J}}_D^v$ in (11) so that

$$\underline{\widetilde{E}}^{v,\Gamma} = \underline{E}_B^{v,\Gamma} + \underline{\underline{G}}_B^{\Gamma}\,\underline{\widetilde{J}}_D^{v} \tag{21}$$

($v = 1, \ldots, V$).

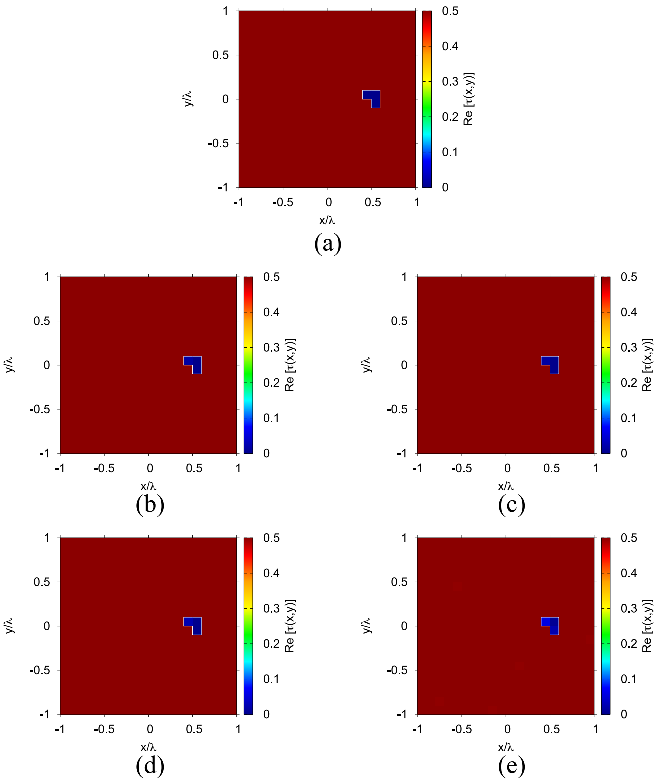

FIGURE 2. Numerical assessment (L-shaped profile, $S = 1$, $P = 3$, $\varepsilon_{r\Psi} = 1.0$, $\sigma_{\Psi} = 0.0$ [S/m], $\tau_{\Psi} = 0.0$, $\varepsilon_{rB} = 1.5$, $\sigma_B = 0.0$ [S/m], $\tau_B = 0.5$, $L = 2.0$ [λ], $N = 400$). (a) Actual and (b)–(e) MT-BCS retrieved contrast when processing noisy data with (b) SNR = 50 [dB], (c) SNR = 20 [dB], (d) SNR = 15 [dB], and (e) SNR = 10 [dB].

IV. NUMERICAL AND EXPERIMENTAL ASSESSMENT

This section is aimed at assessing the proposed MT-BCS method for microwave NDT/NDE. Toward this end, a set of representative numerical (Sections IV-A and IV-B) and experimental (Section IV-C) test cases from an exhaustive validation are reported to show its behavior as well as to point out its potentialities and current limitations. Such an assessment is completed by some comparisons with competitive state-of-the-art inversion techniques (Section IV-B).

To provide a quantitative index on the inversion accuracy, the following integral errors ($\Theta \in \{\text{tot, int, ext}\}$)

$$\xi_{\Theta} = \frac{1}{\text{Area}(\Gamma_{\Theta})} \int_{\Gamma_{\Theta}} \frac{|\tau(\mathbf{r}) - \widetilde{\tau}(\mathbf{r})|}{|\tau(\mathbf{r}) + 1|} d\mathbf{r} \tag{22}$$

have been evaluated, $\tau(\mathbf{r})$ and $\widetilde{\tau}(\mathbf{r})$ being the actual and the retrieved (20) contrast distributions, respectively, while $\Gamma_{\text{tot}} = \Gamma$ (i.e., whole domain), $\Gamma_{\text{int}} = \Psi$ (i.e., the unknown object support), and $\Gamma_{\text{ext}} = (\Gamma \backslash \Psi)$ (i.e., the surrounding background).

A. NUMERICAL ASSESSMENT

As for the numerical assessment, a square investigation domain of side $L = 2$ [λ], λ being the free-space wavelength,

TABLE 1. Numerical assessment (L-shaped profile, $S = 1$, $P = 3$, $\varepsilon_{r\Psi} = 1.0$, $\sigma_{\Psi} = 0.0$ [S/m], $\tau_{\Psi} = 0.0$, $\varepsilon_{rB} = 1.5$, $\sigma_B = 0.0$ [S/m], $\tau_B = 0.5$, $L = 2.0$ [λ], $N = 400$, SNR $\in$ [10, 50] [dB])—integral errors versus *SNR*.

SNR [dB]	ξ_{tot}	ξ_{int}	ξ_{ext}
50	1.23×10^{-4}	1.64×10^{-2}	0.0
20	1.27×10^{-4}	1.69×10^{-2}	0.0
15	1.68×10^{-4}	2.13×10^{-2}	7.65×10^{-6}
10	4.03×10^{-4}	3.18×10^{-2}	1.66×10^{-4}

has been illuminated by $V = 18$ different directions and $M = 18$ ideal probes have been located at the locations

$$(x_m, y_m) = \left(2 \times \cos\left[(m-1)\frac{2\pi}{M}\right][\lambda]\right.$$
$$\left. 2 \times \sin\left[(m-1)\frac{2\pi}{M}\right][\lambda]\right). \tag{23}$$

($m = 1, \ldots, M$) to collect the scattering data in the observation domain Ω. To avoid the “inverse-crime” [1], the investigation domain Γ has been partitioned in $N' = 1600$ and $N = 400$ subdomains in the forward and the inverse problems, respectively. The MT-BCS control parameters (γ_1, γ_2) in (18) have been set according to the guidelines in [36] and the robustness of the MT-BCS has been assessed by blurring the scattered data with an additive white Gaussian noise characterized by a signal-to-noise ratio (SNR).

The first synthetic benchmark [Fig. 2(a)] is concerned with the retrieval of a single ($S = 1$, S being the number of scatterers/disconnected regions in Ψ) *L-shaped* crack ($\varepsilon_{r\Psi} = 1$, $\sigma_{\Psi} = 0.0$ [S/m] $\Rightarrow \tau_{\Psi} = [\varepsilon_{r\Psi} - 1] - j(\sigma_{\Psi}/\omega\varepsilon_0) = 0.0$) of side $\ell = 0.2$ [λ] and embedded within a homogeneous lossless ($\sigma_B = 0.0$ [S/m]) background medium with relative permittivity $\varepsilon_{rB} = 1.5$ ($\Rightarrow \tau_B = 0.5$). In this case, the sparsity index P ($P \triangleq \|\underline{J}_D^v\|_0$, $P << N$, $v = 1, \ldots, V$, $\|.\|_0$ being the ℓ_0-norm) is equal to $P = 3$. Fig. 2 shows the dielectric profiles retrieved with the MT-BCS method when processing blurred data (SNR $\in$ [10, 50] [dB]). As it can be observed, the crack position and its shape are always faithfully recovered independently on the amount of noise. Slight inaccuracies affect the estimated contrasts and negligible artifacts arise in the background region ($\mathbf{r} \in \Gamma_{\text{ext}}$) only when processing highly noisy data [e.g., $\xi_{\text{ext}}|_{\text{SNR}=10\,[\text{dB}]} = 1.66 \times 10^{-4}$—Fig. 2(e)], even though it is still possible to correctly identify/shape the unknown scatterer. These outcomes are quantitatively confirmed by the values of the integral errors in Table 1 where the total error increases of a factor 3.27 when increasing the noise level, passing from SNR = 50 [dB] [Fig. 2(b)] to SNR = 10 [dB] [Fig. 2(e)], while $\xi_{\text{ext}} = 0$ when SNR $\geq$ 20 [dB].

The dependence of the MT-BCS inversion on the properties of the host medium has been assessed next. Toward this purpose, first, the relative permittivity of the background has been uniformly varied within the range $\varepsilon_{rB} \in [1.5, 5.0]$ and the results in terms of error indexes are reported in Fig. 3. As expected, there is a progressive degradation of the

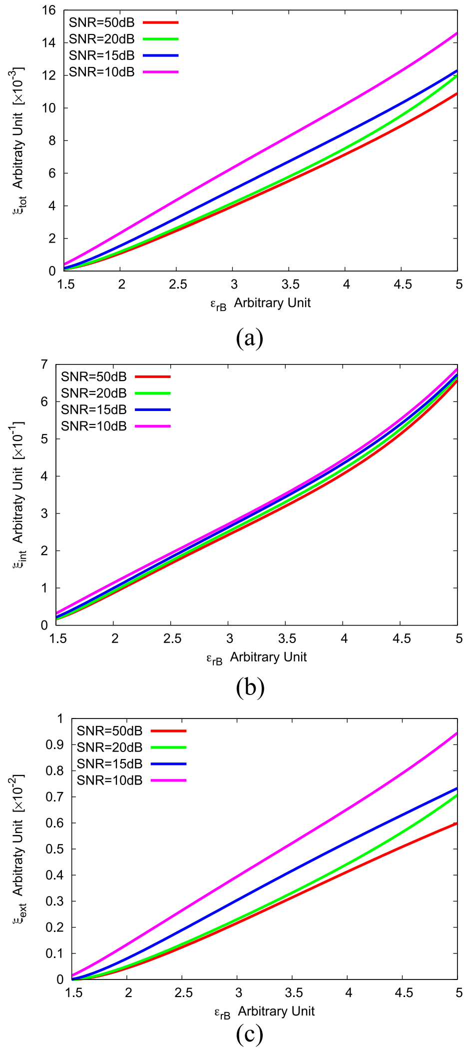

FIGURE 3. **Numerical assessment (L-shaped profile, $S = 1$, $P = 3$, $\varepsilon_{r\Psi} = 1.0$, $\sigma_{\Psi} = 0.0$ [S/m], $\tau_{\Psi} = 0.0$, $\sigma_B = 0.0$ [S/m], $L = 2.0$ [λ], $N = 400$, SNR ∈ [10, 50] [dB]). Behavior of the (a) total (ξ_{tot}), (b) internal (ξ_{int}), and (c) external (ξ_{ext}) integral error as a function of the background relative permittivity, ε_{rB}.**

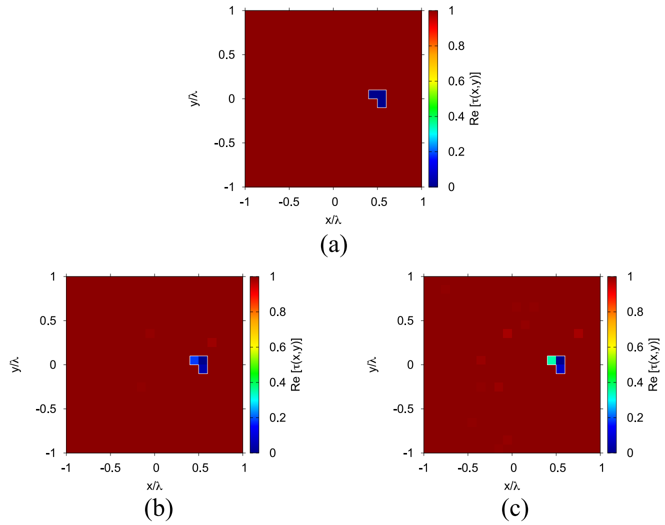

FIGURE 4. **Numerical assessment (L-shaped profile, $S = 1$, $P = 3$, $\varepsilon_{r\Psi} = 1.0$, $\sigma_{\Psi} = 0.0$ [S/m], $\tau_{\Psi} = 0.0$, $\varepsilon_{rB} = 2.0$, $\sigma_B = 0.0$ [S/m], $\tau_B = 1.0$, $L = 2.0$ [λ], $N = 400$). (a) Actual and (b) and (c) MT-BCS retrieved contrast when processing noisy data with (b) SNR = 15 [dB] and (c) SNR = 10 [dB].**

reconstruction accuracy when stronger differential contrasts are at hand [e.g., $|\tau_D|^{\varepsilon_{rB}=1.5} = 0.5 \Rightarrow \xi_{tot}|^{\varepsilon_{rB}=1.5}_{SNR=10\,[dB]} = 4.03 \times 10^{-4}$ versus $|\tau_D|^{\varepsilon_{rB}=2.0} = 1.0 \Rightarrow \xi_{tot}|^{\varepsilon_{rB}=2.0}_{SNR=10\,[dB]} = 2.07 \times 10^{-3}$—Fig. 3(a)]. Nevertheless, faithful qualitative predictions of Γ have been always obtained as pictorially pointed out by the color-maps in Fig. 4 concerned with the case $\varepsilon_{rB} = 2.0$ ($\tau_B = 1.0$) for different and highly blurred data (SNR ∈ [10, 15] [dB]).

As for the inspection of lossy SUTs, the same reference scenario has been imaged by varying the background conductivity between $\sigma_B \in [10^{-6}, 10^{-2}]$ [S/m]. The result is shown in Fig. 5. It can be inferred that the reconstruction is almost independent on the value of σ_B until the threshold value of $\sigma_B^{th} = 10^{-3}$ [S/m] when ($\sigma_B > \sigma_B^{th}$) the error significantly increases. For illustrative purposes, the real and the imaginary parts of the retrieved contrast when SNR = 10 [dB] and $\sigma_B = 10^{-3}$ [S/m] or $\sigma_B = 10^{-2}$ [S/m] are reported in Fig. 6.

Concerning the a-priori assumption that the unknown scattering distribution is sparse w.r.t. the selected pixel basis, the next numerical test is aimed at investigating the case of physically larger scatterers. Toward this end, a set of inversions has been carried out by randomly generating $K = 1600$ random scenarios with objects occupying a total number of pixels in the range $1 \leq P \leq 8$. The outcomes of such a statistical analysis are summarized in Fig. 7 where the average ($\xi_{tot}^{avg} = (1/K)\sum_{k=1}^{K} \xi_{tot}^{k}$), the minimum ($\xi_{tot}^{min} = \min_{k=1,\dots,K} \xi_{tot}^{k}$), and the maximum ($\xi_{tot}^{max} = \max_{k=1,\dots,K} \xi_{tot}^{k}$) values of the total error are shown as a function of P. As expected, the results get worse when larger and larger scatterers have to be imaged because of the increase of the pixel-sparsity order (i.e., $P \uparrow \Rightarrow \xi_{tot}^{avg} \uparrow$), but is also quite interesting to notice that multiple/disconnected (i.e., $S = P$) scatterers are on average more carefully retrieved by the MT-BCS than the single/connected (i.e., $S = 1$) ones (Fig. 7). As a representative example, Fig. 8 shows the actual [Fig. 8(a) and (b)] and reconstructed [Fig. 8(c) and (d)] profiles of random scatterers occupying $P = 6$ pixels. The case with $S = 1$ [Fig. 8(a) versus Fig. 8(c)] turns out to be more complex than that with $S = P$ [Fig. 8(b) versus Fig. 8(d)] as quantitatively confirmed by the comparison between the corresponding internal and external errors (i.e., $[(\xi_{int}|^{S=1}_{SNR=10\,[dB]})/(\xi_{int}|^{S=P}_{SNR=10\,[dB]})] = 2.19$ and $[(\xi_{ext}|^{S=1}_{SNR=10\,[dB]})/(\xi_{ext}|^{S=P}_{SNR=10\,[dB]})] = 1.62$).

Complex-shaped defects can be successfully retrieved, as well, as proven by the color-maps in Fig. 9 related to the *X-shaped* crack of Fig. 9(a). Despite the pixel-sparsity order (i.e., $P = 9$), the shape of the object is always well resolved regardless of the noise level, the external error being equal to 0 when SNR = 50 [dB] (Table 2).

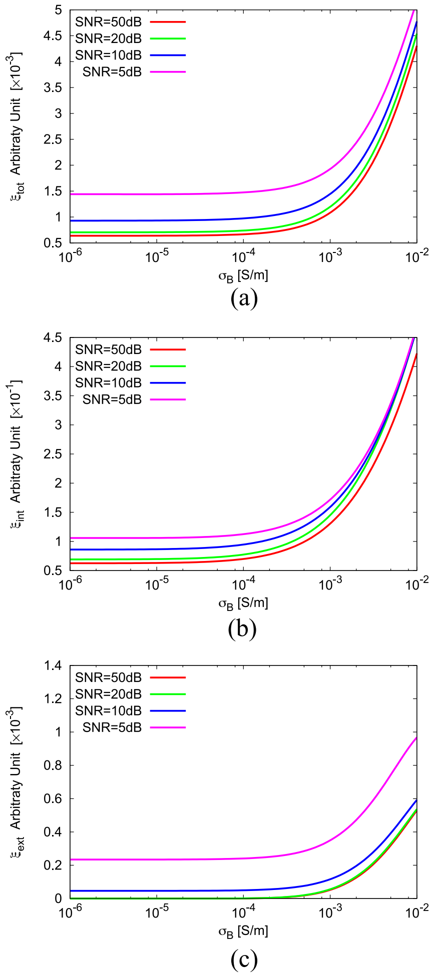

FIGURE 5. Numerical assessment (L-shaped profile, $S = 1$, $P = 3$, $\varepsilon_{r\Psi} = 1.0$, $\sigma_\Psi = 0.0$ [S/m], $\tau_\Psi = 0.0$, $\varepsilon_{rB} = 2.0$, $\sigma_B \in [10^{-6},\ 10^{-2}]$ [S/m], $L = 2.0$ [λ], $N = 400$, SNR $\in [10,\ 50]$ [dB]). Behavior of the (a) total (ξ_{tot}), (b) internal (ξ_{int}), and (c) external (ξ_{ext}) integral error as a function of the background conductivity, σ_B.

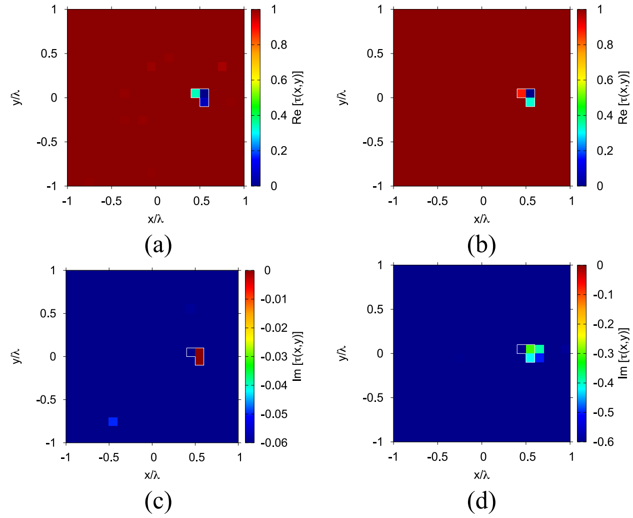

FIGURE 6. Numerical assessment (L-shaped profile, $S = 1$, $P = 3$, $\varepsilon_{r\Psi} = 1.0$, $\sigma_\Psi = 0.0$ [S/m], $\tau_\Psi = 0.0$, $\varepsilon_{rB} = 2.0$, $L = 2.0$ [λ], $N = 400$, SNR = 10 [dB]). (a) and (b) Real part and (c) and (d) imaginary part of the MT-BCS retrieved contrast when the background conductivity is set to (a) and (c) $\sigma_B = 10^{-3}$ [S/m] ($\tau_B = 1.0 - j0.06$) and (b) and (d) $\sigma_B = 10^{-2}$ [S/m] ($\tau_B = 1.0 - j0.6$).

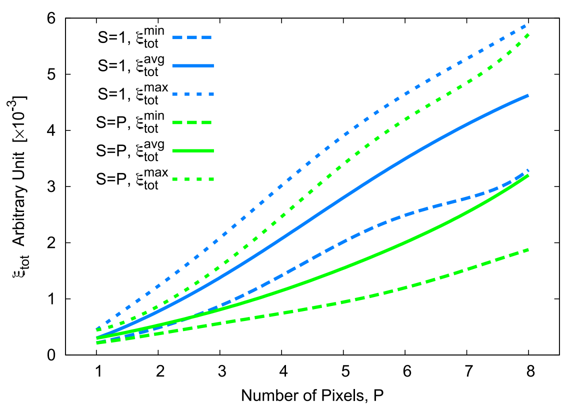

FIGURE 7. Numerical assessment ($\varepsilon_{r\Psi} = 1.0$, $\sigma_\Psi = 0.0$ [S/m], $\tau_\Psi = 0.0$, $\varepsilon_{rB} = 2.0$, $\sigma_B = 0.0$ [S/m], $\tau_B = 1.0$, $L = 2.0$ [λ], $N = 400$, SNR = 10 [dB]). Average (ξ_{tot}^{avg}), minimum (ξ_{tot}^{min}), and maximum (ξ_{tot}^{max}) total error computed over $K = 1600$ random scenarios dealing with a variation of the number of pixels belonging to the scatterer support Ψ (P) and considering single/connected ($S = 1$) or multiple/disconnected ($S = P$) targets.

TABLE 2. Numerical assessment (X-shaped profile, $S = 1$, $P = 9$, $\varepsilon_{r\Psi} = 1.0$, $\sigma_\Psi = 0.0$ [S/m], $\tau_\Psi = 0.0$, $\varepsilon_{rB} = 2.0$, $\sigma_B = 0.0$ [S/m], $\tau_B = 1.0$, $L = 2.0$ [λ], $N = 400$, SNR $\in [10,\ 50]$ [dB])—integral errors versus SNR.

SNR [dB]	ξ_{tot}	ξ_{int}	ξ_{ext}
50	2.35×10^{-3}	9.59×10^{-2}	0.0
20	2.80×10^{-3}	9.81×10^{-2}	6.11×10^{-4}
15	4.26×10^{-3}	1.26×10^{-1}	1.45×10^{-3}
10	6.70×10^{-3}	1.60×10^{-1}	3.17×10^{-3}

The next experiment is devoted to assess the flexibility of the proposed NDT/NDE method, which is not limited to the retrieval of homogeneous cracks, but it can be successfully applied to the more general case of inhomogeneous scatterers, as well. As a proof, the MT-BCS inversions when dealing with the randomly generated scenario of Fig. 10(a) are reported in Fig. 10(b)–(e) ($S = 4$, $P = 6$, $\varepsilon_{r\Psi} \in [1.0,\ 1.8]$). Very accurate predictions of the unknown profile are yielded when SNR ≥ 20 [dB], while there is a slight underestimation of the contrast and minor artifacts appear when processing highly blurred data [e.g., SNR = 10 [dB]—Fig. 10(e)], as quantitatively pointed out by the values of the error indexes in Table 3.

Next, let us now analyze the MT-BCS performance when dealing with nonuniform background media such as the multilayer structure composed by two parallel layers shown in Fig. 11(a) [$\varepsilon_{rB}(x, y) = 2.0$ for $y > 0$ and $\varepsilon_{rB}(x, y) = 3.0$ for $y < 0$]. Despite the more complex scattering scenario, which involves additional reflections at the interface between the two layers, the two actual small cracks [$S = P = 2$—Fig. 11(a)] are correctly detected and localized [i.e., $\xi_{tot}|_{\text{SNR}=15\,[\text{dB}]} = 1.34 \times 10^{-3}$—Fig. 11(c); $\xi_{tot}|_{\text{SNR}=10\,[\text{dB}]} = 1.49 \times 10^{-3}$—Fig. 11(e)]. The effectiveness of the proposed CS-based method in dealing with inhomogeneous backgrounds is also confirmed in the case of an SUT made of two concentric layers

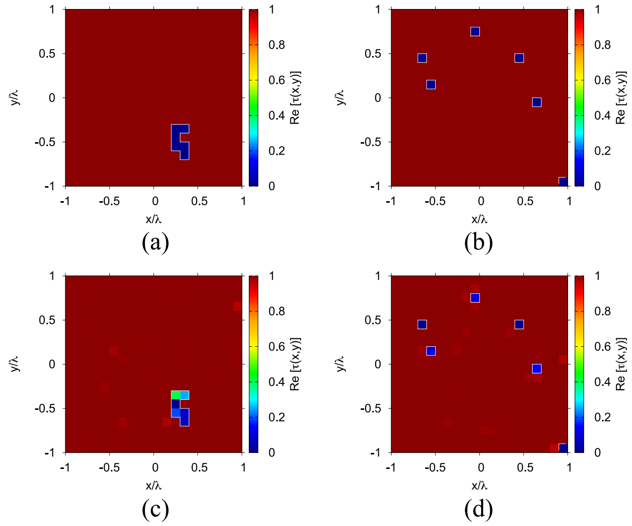

FIGURE 8. Numerical assessment ($P = 6$, $\varepsilon_{r\Psi} = 1.0$, $\sigma_\Psi = 0.0$ [S/m], $\tau_\Psi = 0.0$, $\varepsilon_{rB} = 2.0$, $\sigma_B = 0.0$ [S/m], $\tau_B = 1.0$, $L = 2.0$ [λ], $N = 400$, SNR = 10 [dB]). (a) and (b) Actual and (c) and (d) MT-BCS retrieved contrast when imaging (a) and (c) single/connected ($S = 1$) and (b) and (d) multiple/disconnected ($S = P$) scatterers.

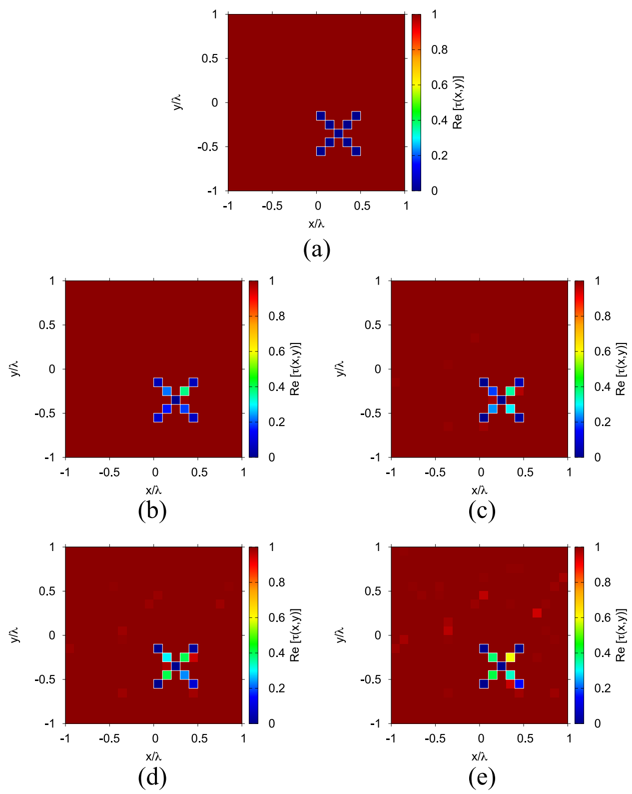

FIGURE 9. Numerical assessment (X-shaped profile, $S = 1$, $P = 9$, $\varepsilon_{r\Psi} = 1.0$, $\sigma_\Psi = 0.0$ [S/m], $\tau_\Psi = 0.0$, $\varepsilon_{rB} = 2.0$, $\sigma_B = 0.0$ [S/m], $\tau_B = 1.0$, $L = 2.0$ [λ], $N = 400$). (a) Actual and (b)–(e) MT-BCS retrieved contrast when processing noisy data with (b) SNR = 50 [dB], (c) SNR = 20 [dB], (d) SNR = 15 [dB], and (e) SNR = 10 [dB].

$[\varepsilon_{rB}(x, y) = 3.0$ for $|x, y| < 0.5\lambda$ and $\varepsilon_{rB}(x, y) = 2.0$ for $|x, y| > 0.5\lambda$—Fig. 11(b)], since $\xi_{\text{tot}}|_{\text{SNR}=15\,[\text{dB}]} = 1.03 \times 10^{-3}$ [Fig. 11(d)] and $\xi_{\text{tot}}|_{\text{SNR}=10\,[\text{dB}]} = 1.61 \times 10^{-3}$ [Fig. 11(f)].

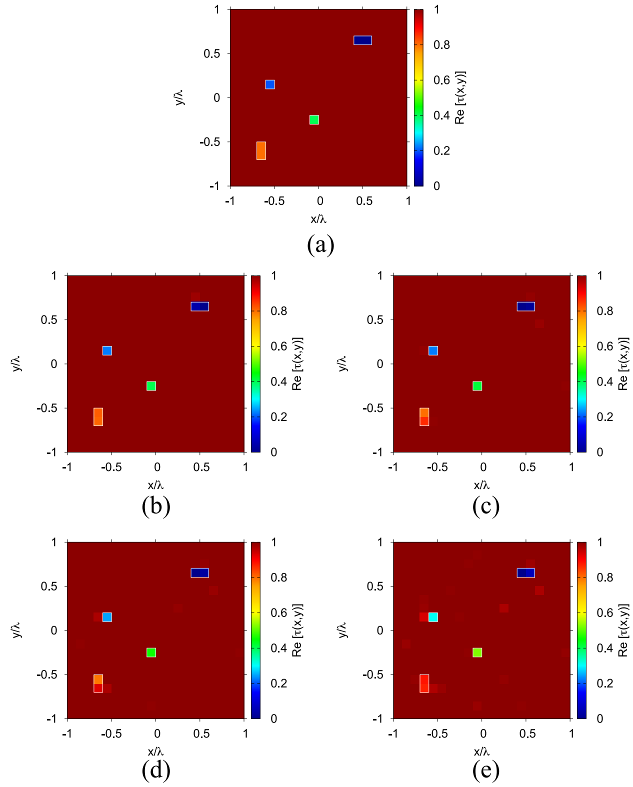

FIGURE 10. Numerical assessment (inhomogeneous profile, $S = 4$, $P = 6$, $\varepsilon_{r\Psi} \in [1.0,\ 1.8]$, $\sigma_\Psi = 0.0$ [S/m], $\varepsilon_{rB} = 2.0$, $\sigma_B = 0.0$ [S/m], $\tau_B = 1.0$, $L = 2.0$ [λ], $N = 400$). (a) Actual and (b)–(e) MT-BCS retrieved contrast when processing noisy data with (b) SNR = 50 [dB], (c) SNR = 20 [dB], (d) SNR = 15 [dB], and (e) SNR = 10 [dB].

TABLE 3. Numerical assessment (inhomogeneous profile, $S = 4$, $P = 6$, $\varepsilon_{r\Psi} \in [1.0,\ 1.8]$, $\sigma_\Psi = 0.0$ [S/m], $\varepsilon_{rB} = 2.0$, $\sigma_B = 0.0$ [S/m], $\tau_B = 1.0$, $L = 2.0$ [λ], $N = 400$, SNR $\in [10,\ 50]$ [dB])—integral errors versus SNR.

SNR [dB]	ξ_{tot}	ξ_{int}	ξ_{ext}
50	5.50×10^{-4}	3.36×10^{-2}	4.66×10^{-5}
20	7.16×10^{-4}	3.91×10^{-2}	1.32×10^{-4}
15	1.20×10^{-3}	5.06×10^{-2}	4.48×10^{-4}
10	2.54×10^{-3}	7.45×10^{-2}	1.44×10^{-3}

It is also interesting to notice that a further increase of the complexity of the imaged domain does not lead to a significant degradation of the reconstructions. For instance, let us consider the case of a three-layered concentric background embedding $S = 3$ scatterers of side $\ell = 0.1$ [λ] [$P = 3$—Fig. 12(a)] and $\ell = 0.2$ [λ] [$P = 12$—Fig. 12(b)], respectively, buried within the inner $[\varepsilon_{rB}(x, y) = 3.0$ for $|x, y| < 0.4\lambda]$, middle $[\varepsilon_{rB}(x, y) = 2.0$ for $0.4\lambda < |x, y| < 0.7\lambda]$, and external $[\varepsilon_{rB}(x, y) = 1.5$ for $|x, y| > 0.7\lambda]$ layers. As shown in the color-maps in Fig. 12, all defects are always correctly detected even though the retrieval accuracy depends on the size (ℓ) of the scatterers that defines their intrinsic sparseness [e.g., $[(\xi_{\text{tot}}|_{\text{SNR}=10\,[\text{dB}]}^{\ell=0.1\,[\lambda]})/(\xi_{\text{tot}}|_{\text{SNR}=10\,[\text{dB}]}^{\ell=0.2\,[\lambda]})] = 0.26$—Fig. 12(d) versus Fig. 12(c)].

Similar conclusions hold when both inhomogeneous scatterers and background are simultaneously present, as well.

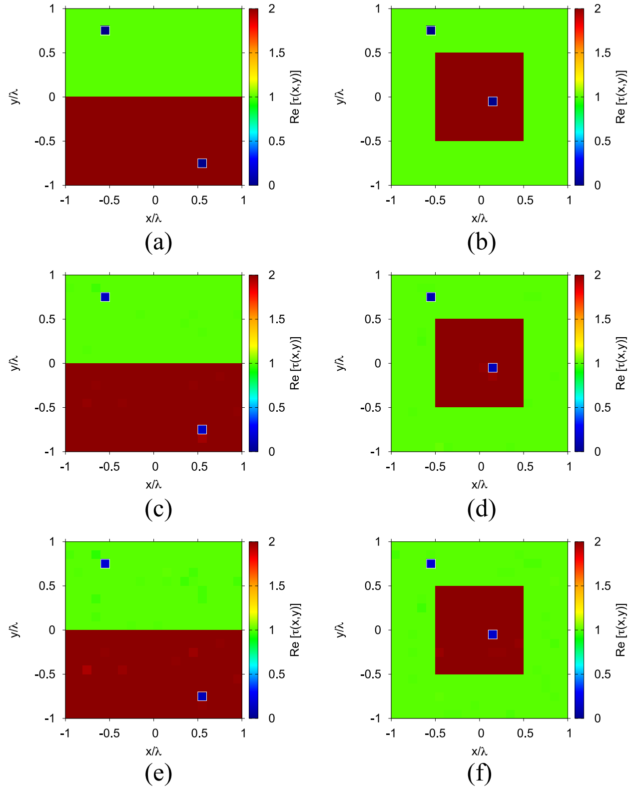

FIGURE 11. Numerical assessment (two-layer scenario, $S = P = 2$, $\varepsilon_{r\Psi} = 1.0$, $\sigma_\Psi = 0.0$ [S/m], $\tau_\Psi = 0.0$, $\varepsilon_{rB} \in [2.0, 3.0]$, $\sigma_B = 0.0$ [S/m], $L = 2.0$ [λ], $N = 400$). (a) and (b) Actual and (c)–(f) MT-BCS retrieved contrast when processing noisy data with (c) and (d) SNR = 15 [dB] and (e) and (f) SNR = 10 [dB] and considering background distributions with (a), (c), and (e) parallel or (b), (d), and (f) concentric layers.

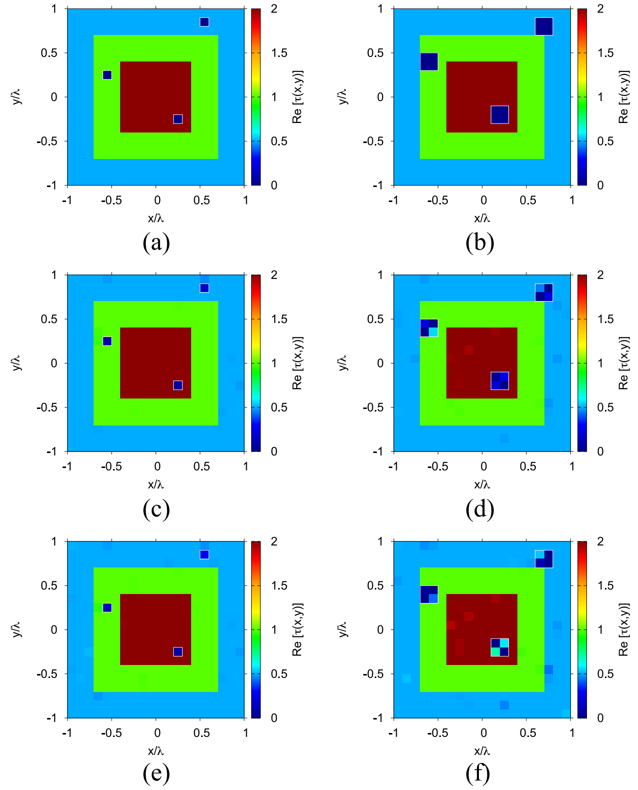

FIGURE 12. Numerical assessment (three-layer scenario, $S = 3$, $\varepsilon_{r\Psi} = 1.0$, $\sigma_\Psi = 0.0$ [S/m], $\tau_\Psi = 0.0$, $\varepsilon_{rB} \in [1.5, 3.0]$, $\sigma_B = 0.0$ [S/m], $L = 2.0$ [λ], $N = 400$). (a) and (b) Actual and (c)–(f) MT-BCS retrieved contrast when processing noisy data with (c) and (d) SNR = 15 [dB] and (e) and (f) SNR = 10 [dB] and considering scatterers of side (a), (c), and (e) $\ell = 0.1$ [λ] ($P = 3$) and (b), (d), and (f) $\ell = 0.2$ [λ] ($P = 12$).

As a matter of fact, the MT-BCS faithfully retrieves an image of Γ when considering both the scenarios depicted in Fig. 13(a) and (b). Regardless of the increased complexity of the imaging scenarios at hand, it turns out that the inhomogeneous scatterers ($\varepsilon_{r\Psi} \in [1.25, 2.0]$) are always correctly detected [Fig. 13(c)–(f)].

Finally, going toward fully realistic NDT/NDE applications, the reconstruction capabilities of the MT-BCS have been assessed when only a partial/imperfect knowledge of the background is available for the reconstruction. More specifically, Fig. 14 presents the obtained outcomes when the actual background has some random variation around the average value, while a homogeneous background (i.e., $\varepsilon_{rB} = 2.0$) has been assumed in the inversion. Assuming a white Gaussian noise on the actual background permittivity values with SNR Υ, it can be inferred that the MT-BCS provides very accurate guesses of the L-shaped scatterer when $\Upsilon = 30$ [dB] [e.g., $\xi_{\text{int}}|_{\text{SNR}=15\,[\text{dB}]}^{\Upsilon=30\,[\text{dB}]} = 7.1 \times 10^{-2}$—Fig. 14(c) versus Fig. 14(a)]. Moreover, the crack is still correctly detected and localized in the very challenging case of $\Upsilon = 20$ [dB] [e.g., $\xi_{\text{int}}|_{\text{SNR}=15\,[\text{dB}]}^{\Upsilon=20\,[\text{dB}]} = 1.4 \times 10^{-1}$—Fig. 14(d) versus Fig. 14(b)].

B. COMPARATIVE ASSESSMENT

To understand the key role of the enforcement of the correlation among the V illuminations in significantly improving the reconstruction accuracy, a comparative assessment has been carried out with the single-task implementation (ST-BCS [46]) of the same probabilistic CS formulation where the multiview data are independently processed. The results of such a comparison are reported in Fig. 15 for the retrieval of the randomly shaped crack in Fig. 15(a). As it can be visually inferred, the MT strategy remarkably overcomes its ST counterpart by yielding more detailed and faithful guesses of the contrast distribution. Indeed, the error improvement is equal to $[(\xi_{\text{tot}}|_{\text{SNR}=10\,[\text{dB}]}^{MT-BCS})/(\xi_{\text{tot}}|_{\text{SNR}=10\,[\text{dB}]}^{ST-BCS})] = 0.15$ [Fig. 15(d) versus Fig. 15(e)]. The advantage of using the MT-BCS over the ST-BCS is even more important when changing the dielectric properties of the background medium as confirmed by the plot of ξ_{tot} versus ε_{rB} in Fig. 16.

The numerical assessment of the MT-BCS has then been completed with a comparison with four non-CS state-of-the-art NDT/NDE solutions based on GAs. Toward this end, the same benchmark dealt with in [33] has been considered. It consists of a square investigation domain ($N = 256$) $L = 0.8$ [λ]-sided with known background properties ($\varepsilon_{rB} = 2.0$ and $\sigma_B = 0.0$ [S/m]) and embedding a single square-shaped crack ($S = 1$, $\tau_\Psi = 0.0$). Analogously to the analysis carried out in [33], a set of reconstructions has been performed by varying the crack area in the range $A_\Psi \in [A_\Psi^{\min}, A_\Psi^{\max}] = [2.5 \times 10^{-3}, 2.5 \times 10^{-1}]$ [λ^2] ($P \in [1, 100]$) and the noise level as SNR $\in [2.5, 30]$ [dB], while evaluating the quality

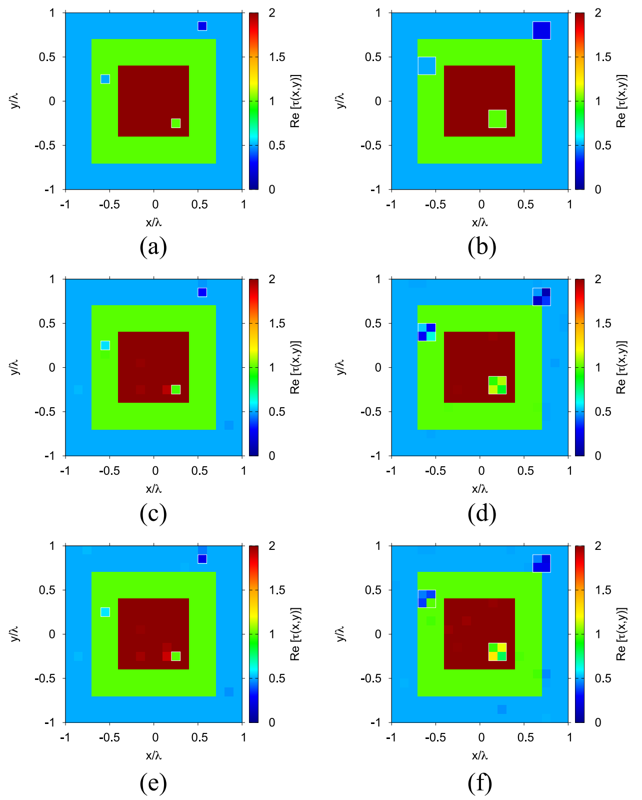

FIGURE 13. Numerical assessment (three-layer scenario with inhomogeneous scatterers, $S = 3$, $\varepsilon_{r\Psi} \in [1.25, 2.0]$, $\sigma_\Psi = 0.0$ [S/m], $\varepsilon_{rB} \in [1.5, 3.0]$, $\sigma_B = 0.0$ [S/m], $L = 2.0$ [λ], $N = 400$). (a) and (b) Actual and (c)–(f) MT-BCS retrieved contrast when processing noisy data with (c) and (d) SNR = 15 [dB] and (e) and (f) SNR = 10 [dB] and considering scatterers of side (a), (c), and (e) $\ell = 0.1$ [λ] ($P = 3$) and (b), (d), and (f) $\ell = 0.2$ [λ] ($P = 12$).

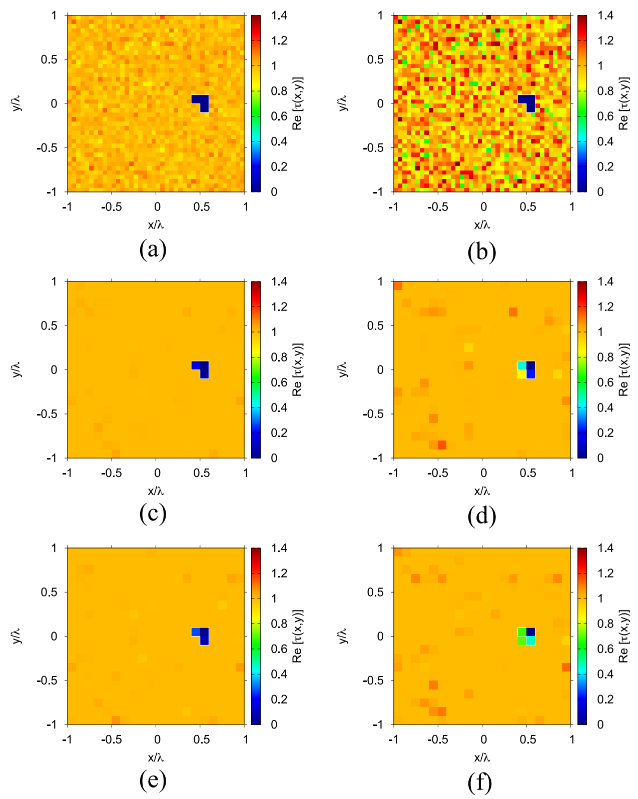

FIGURE 14. Numerical assessment (noisy-background scenario, $S = 1$, $P = 3$, $\varepsilon_{r\Psi} = 1.0$, $\sigma_\Psi = 0.0$ [S/m], $\varepsilon_{rB} = 2.0$, $\sigma_B = 0.0$ [S/m], $L = 2.0$ [λ], $N = 400$). (a) and (b) Actual and (c)–(f) MT-BCS retrieved contrast for (a), (c), and (e) $\Upsilon = 30$ [dB] and (b), (d), and (f) $\Upsilon = 20$ [dB] when processing noisy data with (c) and (d) SNR = 15 [dB] and (e) and (f) SNR = 10 [dB].

of the NDT/NDE diagnoses in terms of the crack localization error [31]

$$\delta = \frac{\sqrt{(x_\Psi - \widetilde{x}_\Psi)^2 + (y_\Psi - \widetilde{y}_\Psi)^2}}{L\sqrt{2}} \times 100. \tag{24}$$

(x_Ψ, y_Ψ) and $(\widetilde{x}_\Psi, \widetilde{y}_\Psi)$ being the actual barycenter and the retrieved one of Ψ, respectively. As it can be inferred from the plots in Fig. 17, the MT-BCS [Fig. 17(a)] overcomes the FGA [31] [Fig. 17(b)], the IGA [32] [Fig. 17(c)], the SMW_U [33] [Fig. 17(d)], and the SMW_B [33] [Fig. 17(e)] when dealing with small cracks ($A_\Psi \leq 5 \times 10^{-2}$ [λ^2]) and highly blurred data (SNR ≤ 20 [dB]), while the performance is comparable in the remaining cases (i.e., $A_\Psi > 5 \times 10^{-2}$ [λ^2]). As a matter of fact, it turns out that when SNR = 2.5 [dB] and $A_\Psi = A_\Psi^{\min}$ only the MT-BCS localization error is null and remarkably lower than the other methods (Table 4). Similar positive outcomes can be also drawn when evaluating the crack area estimation error [31]

$$\eta = \frac{A_\Psi - \widetilde{A}_\Psi}{A_\Psi} \times 100. \tag{25}$$

$\widetilde{A}_\Psi$ being the retrieved area of the defect. As a matter of fact, the MT-BCS clearly takes advantage of *sparseness priors* [Fig. 18(a)] when small defects are at hand. Increasing

TABLE 4. Comparative assessment ($S = 1$, $P \in [1, 100]$, $\varepsilon_{r\Psi} = 1.0$, $\sigma_\Psi = 0.0$ [S/m], $\tau_\Psi = 0.0$, $\varepsilon_{rB} = 2.0$, $\sigma_B = 0.0$ [S/m], $\tau_B = 1.0$, $L = 0.8$ [λ], $N = 256$)—error metrics at SNR = 2.5 [dB].

	$MT-BCS$	FGA	IGA	SMW_U	SMW_B
$\delta\left(A_\Psi^{\min}\right)$	0.00	22.66	41.34	34.18	37.39
$\eta\left(A_\Psi^{\max}\right)$	60.46	34.00	34.00	33.04	35.99

the crack dimensions leads—as expected—to a degradation of the results with respect to the GA-based alternatives [Fig. 18(b)–(e)] since, as $A_\Psi \rightarrow A_\Psi^{\max}$, the differential currents become less and less sparse in the pixel-basis ($P \rightarrow N$). More in detail, when $A_\Psi = A_\Psi^{\max}$ (i.e., $P = 100 \Rightarrow (P/N) = 39\%$) the errors at SNR = 2.5 [dB] made by the MT-BCS are always more than 1.6 times higher than the other techniques (Table 4).

As for the inversion time, Δt, the MT-BCS outperforms all GA-based alternatives since the time saving ($\Delta t^{\text{sav}} = [(\Delta t - \Delta t_{MT-BCS})/\Delta t]$ turns out to be $\Delta t^{\text{sav}}|_{FGA} = 94.69\%$, $\Delta t^{\text{sav}}|_{IGA} = 69.28\%$, $\Delta t^{\text{sav}}|_{SMW_U} = 98.75\%$, and $\Delta t^{\text{sav}}|_{SMW_B} = 97.01\%$ (Table 5), respectively.

C. EXPERIMENTAL ASSESSMENT

The last set of experiments is concerned with experimental data. More specifically, the scattering data are those of the Fresnel Institute of Marseille [47] collected when probing

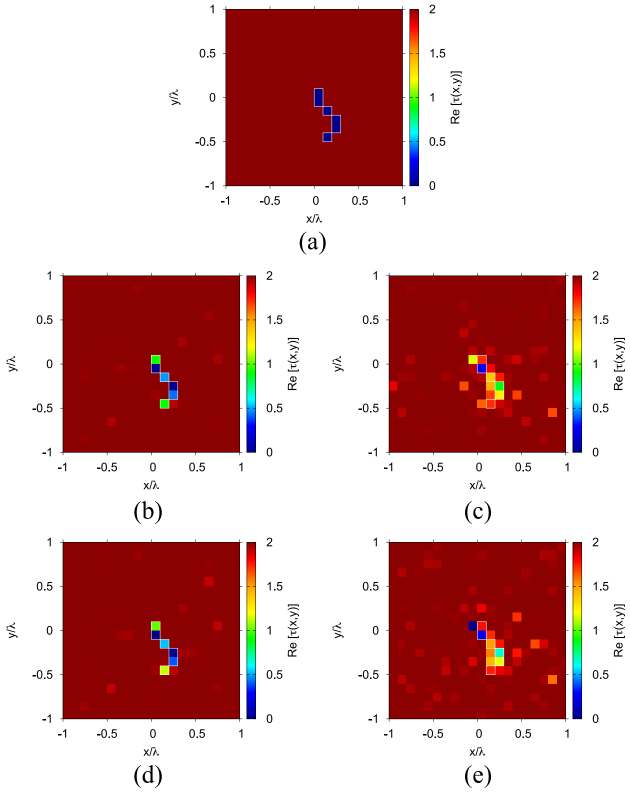

FIGURE 15. Comparative assessment (random-shaped profile, $S = 1$, $P = 6$, $\varepsilon_{r\Psi} = 1.0$, $\sigma_{\Psi} = 0.0$ [S/m], $\tau_{\Psi} = 0.0$, $\varepsilon_{rB} = 3.0$, $\sigma_B = 0.0$ [S/m], $\tau_B = 2.0$, $L = 2.0$ [λ], $N = 400$). (a) Actual and (b)–(e) retrieved contrast by the (b) and (d) MT-BCS and (c) and (e) ST-BCS methods when processing noisy data with (b) and (c) SNR = 15 [dB] and (d) and (e) SNR = 10 [dB].

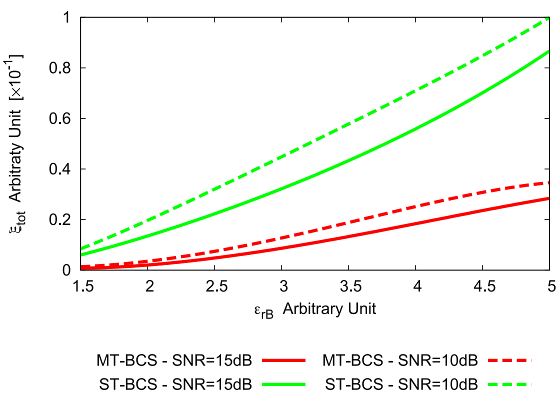

FIGURE 16. Comparative assessment (random-shaped profile, $S = 1$, $P = 6$, $\varepsilon_{r\Psi} = 1.0$, $\sigma_{\Psi} = 0.0$ [S/m], $\tau_{\Psi} = 0.0$, $\varepsilon_{rB} =\in [1.5, 5.0]$, $\sigma_B = 0.0$ [S/m], $L = 2.0$ [λ], $N = 400$, SNR $\in [10, 15]$ [dB]). Behavior of the total integral error, ξ_{tot}, as a function of the background relative permittivity, ε_{rB}, for the MT-BCS and the ST-BCS methods.

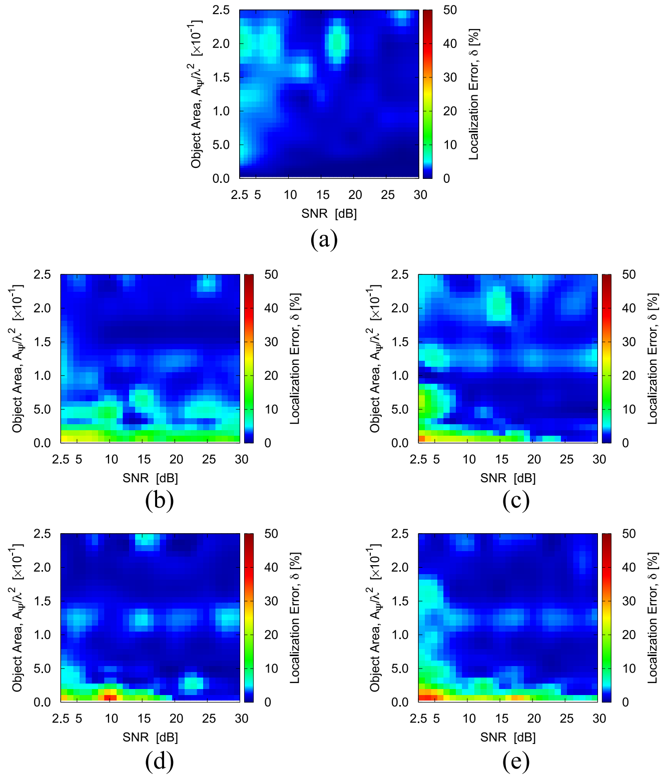

FIGURE 17. Comparative assessment ($S = 1$, $P \in [1, 100]$, $\varepsilon_{r\Psi} = 1.0$, $\sigma_{\Psi} = 0.0$ [S/m], $\tau_{\Psi} = 0.0$, $\varepsilon_{rB} = 2.0$, $\sigma_B = 0.0$ [S/m], $\tau_B = 1.0$, $L = 0.8$ [λ], $N = 256$, SNR $\in [2.5, 30]$ [dB]). Behavior of the crack localization error, δ, as a function of the SNR and the scatterer area, A_Ψ, for the (a) MT-BCS, (b) FGA [31], (c) IGA [32], (d) SMW_U [33], and (e) SMW_B [33] methods.

TABLE 5. Comparative assessment ($S = 1$, $P \in [1, 100]$, $\varepsilon_{r\Psi} = 1.0$, $\sigma_{\Psi} = 0.0$ [S/m], $\tau_{\Psi} = 0.0$, $\varepsilon_{rB} = 2.0$, $\sigma_B = 0.0$ [S/m], $\tau_B = 1.0$, $L = 0.8$ [λ], $N = 256$)—average inversion times.

	$MT-BCS$	FGA	IGA	SMW_U	SMW_B
Δt [sec]	3.05	5.74×10^1	9.93	2.44×10^2	1.02×10^2

a plastic cylinder of diameter $d_1 = 3.1 \times 10^{-2}$ [m] and contrast $\tau_1 = 2.0$ embedded within an external foam cylinder of diameter $d_2 = 8.0 \times 10^{-2}$ [m] and contrast $\tau_2 = 0.45$ [*FoamDielInt*—Fig. 19(a)]. The probing source was a wideband ridged horn working at $f = 2$ [GHz], while $V = 8$ illuminations and $M = 241$ measurement locations have been considered [47].

By assuming the a-priori knowledge of the external foam cylinder, the inner core has been reconstructed with the MT-BCS [Fig. 19(b)] and the ST-BCS [Fig. 19(c)]. While both Bayesian CS (BCS) implementations are able to detect and correctly localize the dielectric inclusion, there is a non-negligible advantage in using the MT approach since the ST one underestimates the contrast and the image of Γ presents some artifacts [Fig. 19(c) versus Fig. 19(b)]. Quantitatively, the values of the integral error are: $\xi_{tot}|^{MT-BCS} = 5.13 \times 10^{-3}$ [Fig. 19(b) versus Fig. 19(a)] and $\xi_{tot}|^{ST-BCS} = 1.36 \times 10^{-2}$ [Fig. 19(c) versus Fig. 19(a)]. For completeness, it is also worth highlighting the computational efficiency of the MT-BCS w.r.t. the ST-BCS since $\Delta t|_{MT-BCS} = 22.9$ [sec] versus $\Delta t|_{ST-BCS} = 36.5$ [sec] ($\Rightarrow \Delta t^{sav}|_{ST-BCS} = 37.26\%$) thanks to the joint processing of the multiview data.

V. CONCLUSION

A novel CS-based MI technique for NDT/NDE has been presented. The proposed method is based on a *differential* formulation of the scattering equations governing the EM interactions between the SUT and the impinging fields. Suitable sparseness regularizers have been profitably

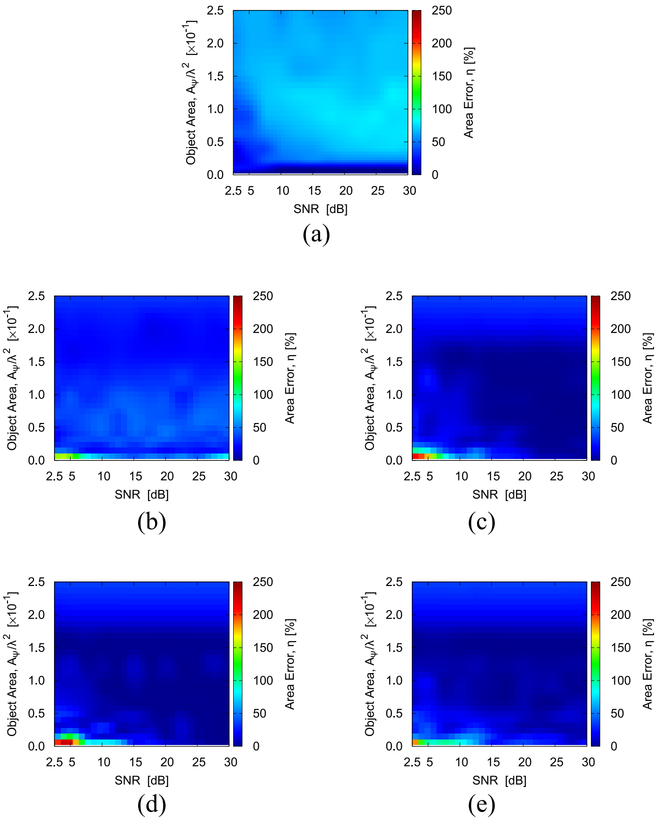

FIGURE 18. **Comparative assessment ($S = 1$, $P \in [1, 100]$, $\varepsilon_{r\Psi} = 1.0$, $\sigma_\Psi = 0.0$ [S/m], $\tau_\Psi = 0.0$, $\varepsilon_{rB} = 2.0$, $\sigma_B = 0.0$ [S/m], $\tau_B = 1.0$, $L = 0.8$ [λ], $N = 256$, SNR $\in [2.5, 30]$ [dB]). Behavior of the crack area estimation error, η, as a function of the SNR and the scatterer area, A_Ψ, for the (a) MT-BCS, (b) FGA [31], (c) IGA [32], (d) SMW_U [33], and (e) SMW_B [33] methods.**

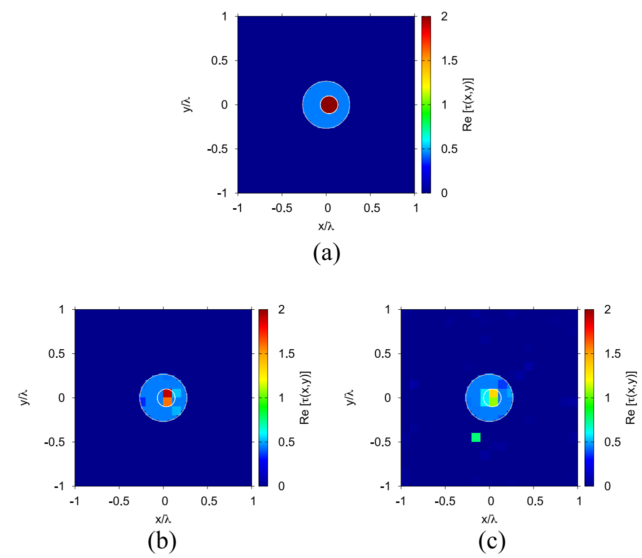

FIGURE 19. **Experimental assessment (*FoamDielInt* profile [47], $f = 2.0$ [GHz], $L = 2.0$ [λ], $N = 400$). (a) Actual and (b) and (c) retrieved contrast by the (b) MT-BCS and (c) ST-BCS methods.**

exploited by solving the differential ISP within a *BCS* framework and enforcing the existing correlation between the contrast sources induced by different illuminations.

From a methodological point of view, to the best of the authors' knowledge, the key novelties of this work include 1) the formulation of the NDT/NDE problem in a *differential* CSI probabilistic framework to exploit the a-priori knowledge of the unperturbed scenario and 2) a suitable customization of the MT-BCS inversion approach to retrieve the differential current induced within arbitrary inhomogeneous structures.

The numerical and experimental assessment has shown that the proposed method:

1) provides accurate guesses of the SUT status with a remarkable robustness to the noise in many heterogeneous scenarios concerned with different scatterers and single/multilayered backgrounds;
2) is not limited to the retrieval of cracks with predetermined shape since it can handle arbitrarily shaped and disconnected defects with inhomogeneous EM properties;
3) remarkably outperforms its "naive" implementation based on a single-task formulation (ST-BCS) when applied to NDT/NDE;
4) positively compares with state-of-the-art (non-CS) inversion methods based on stochastic optimization approaches in terms of both reconstruction accuracy and computational burden;
5) has been successfully applied to experimental data.

Future works, beyond the scope of this article, will be aimed at extending the proposed method to 3-D NDT/NDE problems as well as at its integrations with iterative multiresolution techniques to also exploit the progressively acquired information beyond that on the target sparsity [27]. Moreover, proper reformulations of the differential CSI framework allowing to enforce the correlation between the real and imaginary parts of the sparse differential contrast currents (as done for free-space targets in [22]) will be investigated. Finally, as for the current limitations of the proposed method, it has been shown that the MT-BCS performance degrades when considering the retrieval of large cracks since they are not compliant with the basic assumption of sparsity (in the adopted representation basis). To overcome such a limitation, the imaging of nonsparse objects in the pixel basis through the exploitation of alternative representations (e.g., wavelets [39]) will be the object of future research.

ACKNOWLEDGMENT

Andrea Massa wishes to thank E. Vico for her never-ending inspiration, support, guidance, and help.

REFERENCES

[1] X. Chen, *Computational Methods for Electromagnetic Inverse Scattering*. Singapore: Wiley-IEEE, 2018.
[2] S. S. Ahmed, A. Schiessl, F. Gumbmann, M. Tiebout, S. Methfessel, and L. Schmidt, "Advanced microwave imaging," *IEEE Microw. Mag.*, vol. 13, no. 6, pp. 26–43, Sep./Oct. 2012.

[3] R. Guo et al., "Three dimensional microwave data inversion in feature space for stroke imaging," *IEEE Trans. Med. Imag.*, vol. 43, no. 4, pp. 1365–1376, Apr. 2024, doi: 10.1109/TMI.2023. 3336788.

[4] A. Fedeli, V. Schenone, A. Randazzo, M. Pastorino, T. Henriksson, and S. Semenov, "Nonlinear S-parameters inversion for stroke imaging," *IEEE Trans. Microw. Theory Techn.*, vol. 69, no. 3, pp. 1760–1771, Mar. 2021.

[5] Y. Gao and R. Zoughi, "Millimeter wave reflectometry and imaging for noninvasive diagnosis of skin burn injuries," *IEEE Trans. Instrum. Meas.*, vol. 66, no. 1, pp. 77–84, Jan. 2017.

[6] Y. Qin, T. Rodet, M. Lambert, and D. Lesselier, "Microwave breast imaging with prior ultrasound information," *IEEE Open J. Antennas Propag.*, vol. 1, pp. 472–482, 2020.

[7] A. M. Abbosh, B. Mohammed, and K. S. Bialkowski, "Differential microwave imaging of the breast pair," *IEEE Antennas Wireless Propag. Lett.*, vol. 15, pp. 1434–1437, 2016.

[8] V. Schenone, C. Estatico, G. L. Gragnani, M. Pastorino, A. Randazzo, and A. Fedeli, "Microwave-based subsurface characterization through a combined finite element and variable exponent spaces technique," *Sensors*, vol. 23, no. 1, pp. 1–19, Dec. 2022.

[9] J. D. Chisum and Z. Popovic, "Performance limitations and measurement analysis of a near-field microwave microscope for nondestructive and subsurface detection," *IEEE Trans. Microw. Theory Techn.*, vol. 60, no. 8, pp. 2605–2615, Aug. 2012.

[10] M. Fallahpour and R. Zoughi, "Fast 3-D qualitative method for through-wall imaging and structural health monitoring," *IEEE Geosci. Remote Sens. Lett.*, vol. 12, no. 12, pp. 2463–2467, Dec. 2015.

[11] Y. Chu et al., "Fast microwave through wall imaging method with inhomogeneous background based on Levenberg-Marquardt algorithm," *IEEE Trans. Microw. Theory Techn.*, vol. 67, no. 3, pp. 1138–1147, Mar. 2019.

[12] R. Zoughi, *Microwave Nondestructive Testing and Evaluation*. Amsterdam, The Netherlands: Kluwer, 2000.

[13] S. Kharkovsky and R. Zoughi, "Microwave and millimeter wave nondestructive testing and evaluation-overview and recent advances," *IEEE Instrum. Meas. Mag.*, vol. 10, no. 2, pp. 26–38, Apr. 2007.

[14] Z. Liu, D. Lesselier, and Y. Zhong, "Electromagnetic imaging of damages in fibered layered laminates via equivalence theory," *IEEE Trans. Comput. Imag.*, vol. 4, no. 2, pp. 219–227, Jun. 2018.

[15] J. R. Gallion and R. Zoughi, "Millimeter-wave imaging of surface-breaking cracks in steel with severe surface corrosion," *IEEE Trans. Instrum. Meas.*, vol. 66, no. 10, pp. 2789–2791, Oct. 2017.

[16] O. Mudanyali, S. Yildiz, O. Semerci, A. Yapar, and I. Akduman, "A microwave tomographic approach for nondestructive testing of dielectric coated metallic surfaces," *IEEE Geosci. Remote Sens. Lett.*, vol. 5, no. 2, pp. 180–184, Apr. 2008.

[17] B. Gao, H. Zhang, W. L. Woo, G. Y. Tian, L. Bai, and A. Yin, "Smooth nonnegative matrix factorization for defect detection using microwave nondestructive testing and evaluation," *IEEE Trans. Instrum. Meas.*, vol. 63, no. 4, pp. 923–934, Apr. 2014.

[18] F. Ahmadi, M. T. A. Qaseer, and R. Zoughi, "Microwave nondestructive evaluation of moisture content of polymeric filaments used in additive manufacturing," *IEEE Trans. Instrum. Meas.*, vol. 73, pp. 1–10, 2024, Art. no. 6001910, doi: 10.1109/TIM.2023.3346520.

[19] M. Salucci et al., "Real-time NDT-NDE through an innovative adaptive partial least squares SVR inversion approach," *IEEE Trans. Geosci. Remote Sens.*, vol. 54, no. 11, pp. 6818–6832, Nov. 2016.

[20] G. Dobie, R. Summan, S. G. Pierce, W. Galbraith, and G. Hayward, "A noncontact ultrasonic platform for structural inspection," *IEEE Sensors J.*, vol. 11, no. 10, pp. 2458–2468, Oct. 2011.

[21] J. Helander, A. Ericsson, M. Gustafsson, T. Martin, D. Sjoberg, and C. Larsson, "Compressive sensing techniques for mm-wave nondestructive testing of composite panels," *IEEE Trans. Antennas Propag.*, vol. 65, no. 10, pp. 5523–5531, Oct. 2017.

[22] L. Poli, G. Oliveri, F. Viani, and A. Massa, "MT-BCS-based microwave imaging approach through minimum-norm current expansion," *IEEE Trans. Antennas Propag.*, vol. 61, no. 9, pp. 4722–4732, Sep. 2013.

[23] Y. Zhong, M. Lambert, D. Lesselier, and X. Chen, "A new integral equation method to solve highly nonlinear inverse scattering problems," *IEEE Trans. Antennas Propag.*, vol. 64, no. 5, pp. 1788–1799, May 2016.

[24] O. M. Bucci and G. Franceschetti, "On the degrees of freedom of scattered fields," *IEEE Trans. Antennas Propag.*, vol. 37, no. 7, pp. 918–926, Jul. 1989.

[25] G. Oliveri, P. Rocca, and A. Massa, "A Bayesian compressive sampling-based inversion for imaging sparse scatterers," *IEEE Trans. Geosci. Remote Sens.*, vol. 49, no. 10, pp. 3993–4006, Oct. 2011.

[26] J. T. Case, M. T. Ghasr, and R. Zoughi, "Nonuniform manual scanning for rapid microwave nondestructive evaluation imaging," *IEEE Trans. Instrum. Meas.*, vol. 62, no. 5, pp. 1250–1258, May 2013.

[27] N. Anselmi, L. Poli, G. Oliveri, and A. Massa, "Iterative multi-resolution Bayesian CS for microwave imaging," *IEEE Trans. Antennas Propag.*, vol. 66, no. 7, pp. 3665–3677, Jul. 2018.

[28] P. Rocca, M. Benedetti, M. Donelli, D. Franceschini, and A. Massa, "Evolutionary optimization as applied to inverse problems," *Inverse Probl.*, vol. 25, pp. 1–41, Dec. 2009.

[29] P. Rocca, G. Oliveri, and A. Massa, "Differential evolution as applied to electromagnetics," *IEEE Antennas Propag. Mag.*, vol. 53, no. 1, pp. 38–49, Feb. 2011.

[30] M. Pastorino, "Stochastic optimization methods applied to microwave imaging: A review," *IEEE Trans. Antennas Propag.*, vol. 55, no. 3, pp. 538–548, Mar. 2007.

[31] S. Caorsi, A. Massa, and M. Pastorino, "A crack identification microwave procedure based on a genetic algorithm for nondestructive testing," *IEEE Trans. Antennas Propag.*, vol. 49, no. 12, pp. 1812–1820, Dec. 2001.

[32] S. Caorsi, A. Massa, M. Pastorino, and M. Donelli, "Improved microwave imaging procedure for nondestructive evaluations of two-dimensional structures," *IEEE Trans. Antennas Propag.*, vol. 52, no. 6, pp. 1386–1397, Jun. 2004.

[33] M. Benedetti, M. Donelli, G. Franceschini, M. Pastorino, and A. Massa, "Effective exploitation of the a priori information through a microwave imaging procedure based on the SMW for NDE/NDT applications," *IEEE Trans. Geosci. Remote Sens.*, vol. 43, no. 11, pp. 2584–2592, Nov. 2005.

[34] M. Salucci, L. Poli, P. Rocca, and A. Massa, "Learned global optimization for inverse scattering problems: Matching global search with computational efficiency," *IEEE Trans. Antennas Propag.*, vol. 70, no. 8, pp. 6240–6255, Aug. 2022.

[35] M. Salucci, M. Arrebola, T. Shan, and M. Li, "Artificial intelligence: New frontiers in real-time inverse scattering and electromagnetic imaging," *IEEE Trans. Antennas Propag.*, vol. 70, no. 8, pp. 6349–6364, Aug. 2022.

[36] L. Poli, G. Oliveri, P. Rocca, and A. Massa, "Bayesian compressive sensing approaches for the reconstruction of two-dimensional sparse scatterers under TE illumination," *IEEE Trans. Geosci. Remote Sens.*, vol. 51, no. 5, pp. 2920–2936, May 2013.

[37] G. Oliveri, M. Salucci, N. Anselmi, and A. Massa, "Compressive sensing as applied to inverse problems for imaging: Theory, applications, current trends, and open challenges," *IEEE Antennas Propag. Mag.*, vol. 59, no. 5, pp. 34–46, Oct. 2017.

[38] A. Massa, P. Rocca, and G. Oliveri, "Compressive sensing in electromagnetics-A review," *IEEE Antennas Propag. Mag.*, vol. 57, no. 1, pp. 224–238, Feb. 2015.

[39] N. Anselmi, G. Oliveri, M. A. Hannan, M. Salucci, and A. Massa, "Color compressive sensing imaging of arbitrary-shaped scatterers," *IEEE Trans. Microw. Theory Techn.*, vol. 65, no. 6, pp. 1986–1999, Jun. 2017.

[40] G. Gottardi, M. A. Hannan, and A. Polo, "NDT/NDE by means of a probabilistic differential compressive sensing method," *J. Phys., Conf. Series*, vol. 1476, no. 1, pp. 1–7, 2020.

[41] M. Li, A. Abubakar, and P. M. Van Den Berg, "Application of the multiplicative regularized contrast source inversion method on 3D experimental fresnel data," *Inverse Probl.*, vol. 25, no. 2, pp. 1–23, 2009.

[42] X. Y. Wang, M. Li, and A. Abubakar, "Acceleration of 2-D multiplicative regularized contrast source inversion algorithm using paralleled computing architecture," *IEEE Antennas Wireless Propag. Lett.*, vol. 16, pp. 441–444, 2017.

[43] J. Richmond, "Scattering by a dielectric cylinder of arbitrary cross section shape," *IEEE Trans. Antennas Propag.*, vol. 13, no. 3, pp. 334–341, May 1965.

[44] S. Ji, D. Dunson, and L. Carin, "Multitask compressive sensing," *IEEE Trans. Signal Process.*, vol. 57, no. 1, pp. 92–106, Jan. 2009.

[45] M. E. Tipping, "Sparse Bayesian learning and the relevant vector machine," *J. Mach. Learn. Res.*, vol. 1, pp. 211–244, Jun. 2001.
[46] S. Ji, Y. Xue, and L. Carin, "Bayesian compressive sensing," *IEEE Trans. Signal Process.*, vol. 56, no. 6, pp. 2346–2356, Jun. 2008.
[47] J. M. Geffrin, P. Sabouroux, and C. Eyraud, "Free space experimental scattering database continuation: Experimental set-up and measurement precision," *Inverse Probl.*, vol. 21, no. 6, pp. S117–S130, Dec. 2005.

MARCO SALUCCI (Senior Member, IEEE) received the M.S. degree in telecommunication engineering from the University of Trento, Trento, Italy, in 2011, and the Ph.D. degree from the International Doctoral School in Information and Communication Technology, University of Trento in 2014.

He was a Postdoctoral Researcher with CentraleSuplec, Paris, France, and a Postdoctoral Researcher with the Commissariat l'Energie Atomique et aux Energies Alternatives, Paris. He is currently an Assistant Professor with the Department of Civil, Environmental, and Mechanical Engineering, University of Trento, and a Research Fellow of the ELEDIA Research Center, Gif-sur-Yvette, France. He co-edited the book *Applications of Deep Learning in Electromagnetics—Teaching Maxwell's Equations to Machines* (IET, 2023). His research activities are mainly concerned with inverse scattering, biomedical and GPR microwave imaging techniques, antenna synthesis, and computational electromagnetics with focus on system-by-design methodologies integrating optimization techniques and artificial intelligence for real-world applications.

Dr. Salucci is an Associate Editor for Communications and Memberships of the IEEE TRANSACTIONS ON ANTENNAS AND PROPAGATION. Moreover, he serves as an Associate Editor for the IEEE TRANSACTIONS ON ANTENNAS AND PROPAGATION, the IEEE OPEN JOURNAL OF ANTENNAS AND PROPAGATION, and the *International Journal of Microwave and Wireless Technologies*. Furthermore, he serves as a reviewer for different international journals, including the IEEE TRANSACTIONS ON ANTENNAS AND PROPAGATION, the IEEE TRANSACTIONS ON MICROWAVE THEORY AND TECHNIQUES, the IEEE TRANSACTIONS ON GEOSCIENCE AND REMOTE SENSING, and the IEEE JOURNAL ON MULTISCALE AND MULTIPHYSICS COMPUTATIONAL TECHNIQUES. He is a member of the IEEE Antennas and Propagation Society and he was a member of the COST Action TU1208 "Civil Engineering Applications of Ground Penetrating Radar."

LORENZO POLI (Senior Member, IEEE) received the M.S. degree in telecommunication engineering from the University of Trento, Trento, Italy, in 2008, and the Ph.D. degree from the International Doctoral School in Information and Communication Technology, University of Trento in 2012.

He is currently an Assistant Professor with the Department of Civil, Environmental, and Mechanical Engineering, University of Trento, and a Research Fellow of the ELEDIA Research Center, Gif-sur-Yvette, France. He was a Visiting Researcher with the Laboratoire des Signaux et Systèmes (L2S@Suplec), Gif-sur-Yvette, in 2015, and a Visiting Professor with the University of Paris Sud, Gif-sur-Yvette, in 2016. He is the author/co-author of more than 60 journals and 90 conference papers. His research activities are focused on the solution of antenna design and unconventional array synthesis problems as well as electromagnetic inverse scattering problems.

Dr. Poli has been a member of the IEEE Antennas and Propagation Society since 2010, when he was a recipient of the IEEE Antennas and Propagation Society Doctoral Research Award. He serves as a Reviewer for several international journals, including IEEE TRANSACTIONS ON ANTENNAS AND PROPAGATION, IEEE ANTENNAS AND WIRELESS PROPAGATION LETTERS, and *IET Microwaves, Antennas & Propagation*.

GIORGIO GOTTARDI received the B.S. degree in electronics and telecommunication engineering and the M.S. degree in telecommunication engineering from the University of Trento, Trento, Italy, in 2012 and 2015, respectively, and the Ph.D. degree from the International Doctoral School in Information and Communication Technology, University of Trento in 2019.

He is currently a Postdoctoral Fellow with the Department of Civil, Environmental and Mechanical Engineering, University of Trento, and a Research Fellow of the ELEDIA Research Center, Gif-sur-Yvette, France. His research activities are mainly focused on synthesis methods for unconventional antenna array architectures for next-generation communications.

GIACOMO OLIVERI (Fellow, IEEE) received the B.S. and M.S. degrees in telecommunications engineering and the Ph.D. degree in space sciences and engineering from the University of Genoa, Genoa, Italy, in 2003, 2005, and 2009, respectively.

He is currently an Associate Professor with the Department of Civil, Environmental, and Mechanical Engineering, University of Trento, Trento, Italy, and a Board Member of the ELEDIA Research Center, Gif-sur-Yvette, France. Moreover, he is an Adjunct Professor with CentraleSuplec, Gif-sur-Yvette, and a member of the Laboratoire des signaux et systmes (L2S)@CentraleSuplec, Gif-sur-Yvette. He has been a Visiting Researcher with L2S in 2012, 2013, and 2015, an Invited Associate Professor with the University of Paris Sud, Gif-sur-Yvette, in 2014, and a Visiting Professor with University Paris-Saclay, Gif-sur-Yvette, in 2016 and 2017. He is the author/co-author of over 400 peer-reviewed papers on international journals and conferences. His research work is mainly focused on electromagnetic direct and inverse problems, metamaterials analysis and design, and antenna array synthesis.

Prof. Oliveri served as an Associate Editor for the IEEE ANTENNAS AND WIRELESS PROPAGATION LETTERS from 2016 to 2022 and the IEEE JOURNAL ON MULTISCALE AND MULTIPHYSICS COMPUTATIONAL TECHNIQUES from 2017 to 2023, and he is an Associate Editor of *EPJ Applied Metamaterials*, the *International Journal of Antennas and Propagation*, the *International Journal of Distributed Sensor Networks*, *Microwave Processing*, and *Sensors*. He has been serving as the Chair for the AP-S IEEE Press Liaison Committee, and a member of the IEEE AP-S Field Award Subcommittee and the IEEE AP-S Membership and Benefit Committee. He is the Chair of the IEEE AP/ED/MTT North Italy Chapter.

LUCA TOSI (Member, IEEE) received the M.S. degree in communication and information engineering from the University of Trento, Trento, Italy, in 2022. He is currently pursuing the Ph.D. degree with the Doctoral Programme in Civil, Environmental and Mechanical Engineering, University of Trento.

His research activity is focused on noninvasive electromagnetic imaging, synthesis and design of unconventional antenna arrays, and quantum computing methodologies for electromagnetic engineering.

ANDREA MASSA (Fellow, IEEE) received the Laurea (M.S.) degree in electronic engineering and the Ph.D. degree in EECS from the University of Genoa, Genoa, Italy, in 1992 and 1996, respectively.

He is currently a Full Professor of Electromagnetic Fields with the University of Trento, Trento, Italy, where he currently teaches electromagnetic fields, inverse scattering techniques, antennas and wireless communications, wireless services and devices, and optimization techniques. He is also currently the Director of the network of federated laboratories "ELEDIA Research Center" located in Brunei, China, Czech, France, Greece, Italy, Japan, Peru, and Tunisia with more than 150 researchers. Moreover, he is a holder of a Chang-Jiang Chair Professorship with the University of Electronic Science and Technology of China (UESTC), Chengdu, China, a Visiting Research Professor with the University of Illinois at Chicago, Chicago, IL, USA, a Visiting Professor with Tsinghua University, Beijing, China, a Visiting Professor with Tel Aviv University, Tel Aviv, Israel, and a Professor with CentraleSuplec, Paris, France. He has been a holder of a Senior DIGITEO Chair with L2S-CentraleSuplec, Gif-sur-Yvette, France, and CEA LIST, Saclay, France, a UC3M-Santander Chair of Excellence with the Universidad Carlos III de Madrid, Madrid, Spain, an Adjunct Professor with Penn State University, University Park, PA, USA, a Guest Professor with UESTC, and a Visiting Professor with the Missouri University of Science and Technology, Rolla, MO, USA; Nagasaki University, Nagasaki, Japan; the University of Paris Sud, Gif-sur-Yvette; Kumamoto University, Kumamoto, Japan; and the National University of Singapore, Singapore. He published more than 900 scientific publications among which more than 350 on international journals (> 15 000 citations H-index = 65 [Scopus]; > 12 000 citations H-index = 59 [ISI-WoS]; > 23 000 citations H-index = 89 [Google Scholar]) and more than 550 in international conferences where he presented more than 200 invited contributions (> 40 invited keynote speaker) (www.eledia.org/publications). He has organized more than 100 scientific sessions in international conferences and has participated to several technological projects in the national and international framework with both national agencies and companies (18 international prj, > 5 MEu; 8 national prj, > 5 MEu; 10 local prj, > 2 MEu; 63 industrial prj, > 10 MEu; 6 university prj, > 300 KEu). His research activities are mainly concerned with inverse problems, analysis/synthesis of antenna systems and large arrays, radar systems synthesis and signal processing, cross-layer optimization and planning of wireless/RF systems, semantic wireless technologies, system-by-design and material-by-design (metamaterials and reconfigurable-materials), and theory/applications of optimization techniques to engineering problems (telecommunications, medicine, and biology).

Prof. Massa serves as an Associate Editor for the *International Journal of Microwave and Wireless Technologies* and he is a member of the Editorial Board of the *Journal of Electromagnetic Waves and Applications*, a permanent member of the "PIERS Technical Committee" and the "EuW Technical Committee," and an ESoA Member. He has been appointed in the Scientific Board of the "Società Italiana di Elettromagnetismo" and elected in the Scientific Board of the Interuniversity National Center for Telecommunications (CNIT). He was appointed as an IEEE AP-S Distinguished Lecturer from 2016 to 2018 and served as an Associate Editor for the IEEE TRANSACTION ON ANTENNAS AND PROPAGATION from 2011 to 2014. He has been appointed in 2011 by the National Agency for the Evaluation of the University System and National Research (ANVUR) as a member of the Recognized Expert Evaluation Group (Area 09, "Industrial and Information Engineering") for the evaluation of the researches at the Italian University and Research Center from 2004 to 2010. Furthermore, he has been elected as the Italian Member of the Management Committee of the COST Action TU1208 "Civil Engineering Applications of Ground Penetrating Radar."

Open Access funding provided by 'Università degli Studi di Trento' within the CRUI CARE Agreement